Disrupted cystine transport via xCT induces serine metabolic reprogramming and enhances differentiation in skeletal muscle cells

Charbel Karam

A thesis submitted to the University of Ottawa
in partial fulfillment of the requirements for the
Master of Science degree in Biochemistry

Department of Biochemistry, Microbiology and Immunology
Faculty of Medicine
University of Ottawa

ABSTRACT

Skeletal muscle (SKM) is a remarkable tissue that exerts many important functions such as maintaining posture and mobility, but also plays a major role in metabolism. SKM health is affected by redox homeostasis, which involves electron transfer between molecules driven by redox pairs that interconvert between oxidized and reduced states. The antioxidant glutathione (GSH) and its oxidized disulfide form (GSSG) is one such redox pair that is very abundant in cells, including muscle stem cells (MuSCs), and therefore generally determines cellular redox state. The synthesis of GSH is limited by the availability of cyst(e)ine, which mostly enters cells through the cystine/glutamate plasma membrane antiporter xCT. The goal of this work was to assess the impact of disrupted cystine import on MuSC health and SKM regeneration (myogenesis). Specifically, the understanding of the specific metabolic implications induced by xCT dysfunction, and their consequence on mitochondrial function and myogenesis was sought. MuSCs from mice harboring a mutation in the *Slc7a11* gene encoding xCT ($Slc7a11^{sut/sut}$) were investigated and findings demonstrated perturbed GSH homeostasis and higher H_2O_2 production compared to WT. Moreover, $Slc7a11^{sut/sut}$ MuSCs had lower mitochondrial oxidative function and higher Drp1-mediated mitochondrial fission. Metabolomics analyses and [U-^{13}C]-glucose stable isotope tracing showed profound metabolic reprogramming in $Slc7a11^{sut/sut}$ MuSCs, characterized by lower TCA cycle activity and increased glucose flux towards *de novo* serine and cysteine synthesis. Finally, $Slc7a11^{sut/sut}$ MuSCs demonstrated higher differentiation and regeneration rates as evidenced by a higher fusion index of myotubes at day 2 of differentiation and increased tissue myofiber cross-sectional area at 21 days post-cardiotoxin injury. Therefore, beyond its established function in

redox homeostasis, this work unravels a critical metabolic function of xCT in muscle cells, providing insights that may inform therapeutic strategies for muscular pathologies.

ACKNOWLEDGEMENTS

The author of this thesis wishes to thank God, Jesus Christ, and the most Holy Spirit for the abundant graces that made this work possible. Thank you to the Blessed Virgin Mary and all the Saints.

The author greatly appreciates the support received from his family.

The author also sends deep gratitude to the support provided by the principal investigator Dr. Mary-Ellen Harper, the PhD candidate Michel Kanaan, the research associate Dr. Chantal Pileggi, and all lab members.

This work was partly funded by the Canadian Institute of Health Research (CIHR) through a Canada Graduate Scholarship-Master's scholarship to the author of this thesis.

Again and again, the author thanks the Lord.

STATEMENT OF CONTRIBUTION

Experiments included in this thesis were conducted in equal collaboration with the PhD candidate, Michel Kanaan.

The author of this thesis participated in all aspects of the experiments mentioned herein, including planning, data gathering, data analysis, and manuscript writing. Some experiments such as H_2O_2 determinations, metabolomics, and immunostaining analyses, were conducted primarily by the author of this thesis, while other experiments such as Seahorse analyses and citrate synthase assay were conducted primarily by Michel Kanaan. All other experiments were conducted equally by both the author and Michel Kanaan.

The PhD Candidate Luke Kennedy performed bioinformatics analyses of unlabeled metabolomics data.

Artificial Intelligence (ChatGPT) was used in this work for the exclusive purpose of assisting with literature searches to find appropriate scientific articles. Some graphics in this work were created with Biorender.

TABLE OF CONTENTS

LIST OF FIGURES

CHAPTER 1: INTRODUCTION

1.1 Skeletal muscle

With extensive training, humans can generate enough force to lift items weighing several times their own body weight. This highlights the remarkable power of skeletal muscle (SKM), which is made possible through the sophisticated coordination between our neuromuscular system and bones. Several diseases affect the function of SKM, and many treatment options are yet to be discovered. First, a brief overview on muscle structure, function, and regenerative capacity is presented.

1.1.1 SKM anatomy

SKM is a contractile tissue under voluntary control and is composed mainly of an arrangement of elongated multi-nucleated muscle fibers, muscle stem cells, and connective tissue. SKM is connected to motor neurons via neuromuscular junctions where actional potentials are transmitted from nerve to muscle, triggering SKM contraction. Within a muscle, which is surrounded by a layer of connective tissue known as the epimysium, groups of myofibers bundle together and are further surrounded by connective tissue known as the perimysium (**Figure 1**) [1].

Individual muscle cells contain billions of organized protein myofilaments forming sarcomeres, which are the contractile units of SKM [1]. The two most abundant proteins are actin and myosin, but there are many other proteins found in SKM like the troponins, tropomyosin, titin, nebulin, α-actinin, desmin, and dystrophin, that play key roles in generating contraction, maintaining the integrity of the sarcomere, and cell signaling [2,3]. Dysfunction in these proteins, for example dystrophin, is often associated with neuromuscular disorders

like Duchenne muscular dystrophy and may result in damage to the SKM structure and function [4].

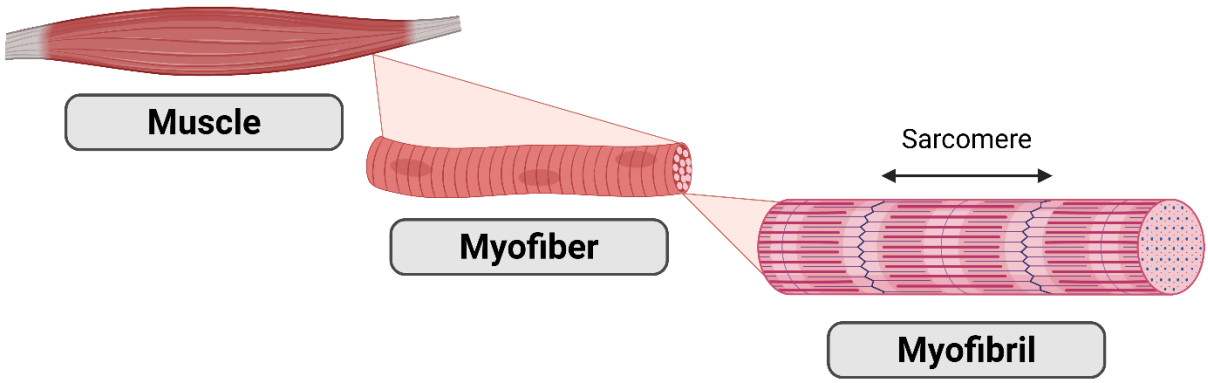

Figure 1. Skeletal muscle anatomy.
A muscle is composed of a bundle of myofiber groups. Each myofiber contains billions of myofibrils which form sarcomeres, the contractile units of SKM.

1.1.2 SKM function and metabolism

SKM has many functions that can be grouped in 2 main categories: contractile and metabolic. Contraction is a complex process that involves the concerted effort of multiple proteins and signaling molecules. Briefly, an action potential in motor neurons reaches the muscle and triggers the release of calcium into the sarcoplasm (cytoplasm of SKM cells). Calcium binds and releases troponin C from blocking the active site of actin filaments, allowing the interaction between actin and myosin ultimately leading to successive sliding of actin and myosin filaments and the generation of force. Importantly, sliding requires the hydrolysis of an ATP molecule, making SKM contraction an energetically demanding process. At rest, SKM contributes about 20% of energy expenditure. While SKM uses more fatty acids than glucose over a 24 h period, it is responsible for ~80% of postprandial (post-meals) glucose uptake, thus playing a crucial role in whole-body glucose metabolism [5].

The metabolic characteristics of SKM further differ between fiber types. Indeed, SKM is heterogenous in its composition, and composed of a selection of fibers such as type I (slow twitch; oxidative), type IIa (fast twitch; oxidative/glycolytic), and type IIb (fast twitch; glycolytic) [6]. Moreover, fiber type characteristics vary between species; for example, in addition to type IIx fibers that are found in mice and humans, mice have type IIb fibers, which are functionally similar to type IIx fibers, but not identical. Commonly, type II fibers have an increasingly faster contraction rate and rely more on glycolysis as a source of ATP. Therefore, type I oxidative fibers have higher mitochondrial content than type IIa, which have higher mitochondrial content than IIb fibers. Interestingly, type IIa fibers sometimes have equal mitochondrial content as type I fibers [7,8].

Mitochondria are cellular energetic hubs, responsible for the production of the majority of cellular ATP by oxidative phosphorylation (OXPHOS), along with various other functions like interconversion of biosynthetic intermediates, energy sensing, and contributing to cellular stress responses [9–12]. Importantly, mitochondria are major players in redox homeostasis, and this will be further examined in the next section.

Mitochondria are dynamic organelles capable of fusion and fission, allowing them to adapt their morphology to the rapidly evolving cellular environment (**Figure 2**). Indeed, as is the case with most biological entities, mitochondrial function is tightly linked to its structure. For example, preventing mitochondrial fusion is linked to decreased exercise performance [13]. Many proteins are involved in the finely tuned choreography of mitochondrial structural remodeling. Mitofusin 1 and 2 (Mfn1/2) and Optic Atrophy 1 (OPA1) are the main regulators of mitochondrial fusion, while Dynamin-related protein 1 (Drp1) is mainly responsible for mitochondrial fission, but other adaptor proteins such as Fis1, Mff, Mid49, and Mid51 are also involved in fission [14,15]. Ultimately, these proteins work in coordination to adapt to various challenging cellular demands, for example throughout SKM regeneration.

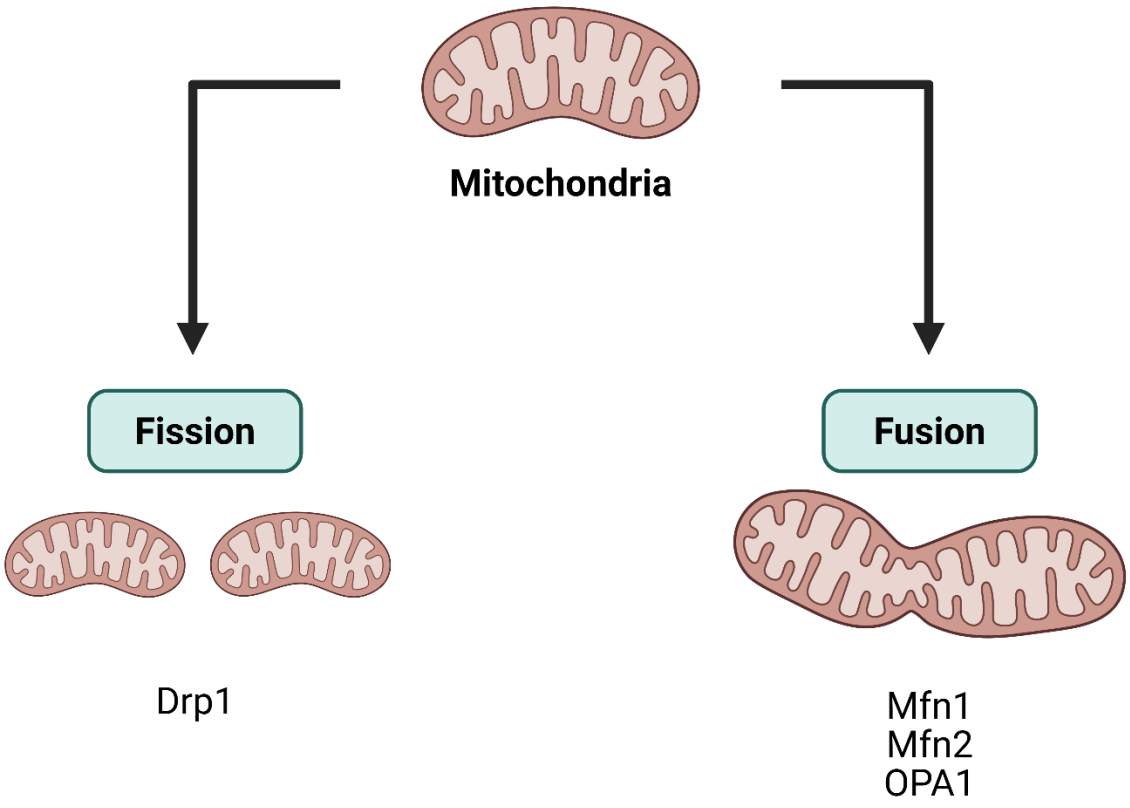

Figure 2. Mitochondrial fission and fusion.
Mitochondria are dynamic organelle that undergo fission, mainly mediated by Drp1, and fusion, mainly mediated by Mfn1/2 and OPA1.

1.1.3 SKM myogenesis

SKM regeneration, termed myogenesis, is a remarkable property of SKM whereby it is able to be restored after damage, such as that resulting from exercise training. Myogenesis occurs both in developing embryos and in adults [16]. This is mainly due to a special population of stem cells called muscle satellite cells (MuSCs) that reside in a quiescent state beneath the basal lamina [17]. Upon activation, MuSCs enter the cell cycle to proliferate, and, while a small subset is used to replenish the MuSC pool, the majority of MuSCs start differentiating and eventually either fuse with each other to form new myofibers, or more commonly, fuse to existing myofibers (**Figure 3**).

At different steps throughout myogenesis, cells express specific transcription factors. For example, in quiescence and early proliferation, Pax7 is expressed. Proliferating MuSCs are characterized by the expression of MyoD [18]. In early differentiation, the expression of Pax7 and MyoD is downregulated and Myogenin is expressed, which is considered a marker of irreversible terminal myogenic differentiation [19]. Finally, fused myotubes express contractile proteins like myosin heavy chain (MHC).

Myogenesis is accompanied by significant metabolic changes. As the activation of MuSCs is energetically demanding [20], MuSCs exiting quiescence and entering proliferation switch from OXPHOS to glycolysis as a major source of ATP production. This metabolic reprogramming towards an inefficient glycolysis (i.e., less ATP per molecule of glucose) offers important advantages for cells, including the ability to rapidly synthesize ATP and generate key metabolic intermediates that are necessary for the synthesis of new molecules [21,22]. Increased amino acid uptake through transporters such as L-type amino acid transporter 1 (LAT1, importing leucine) is also needed to support anabolic processes [23]. Importantly,

myogenesis and SKM metabolism are tightly regulated and affected by perturbations in cellular redox, which is a balance between the production of reactive oxygen and nitrogen species, and their neutralization by antioxidant molecules.

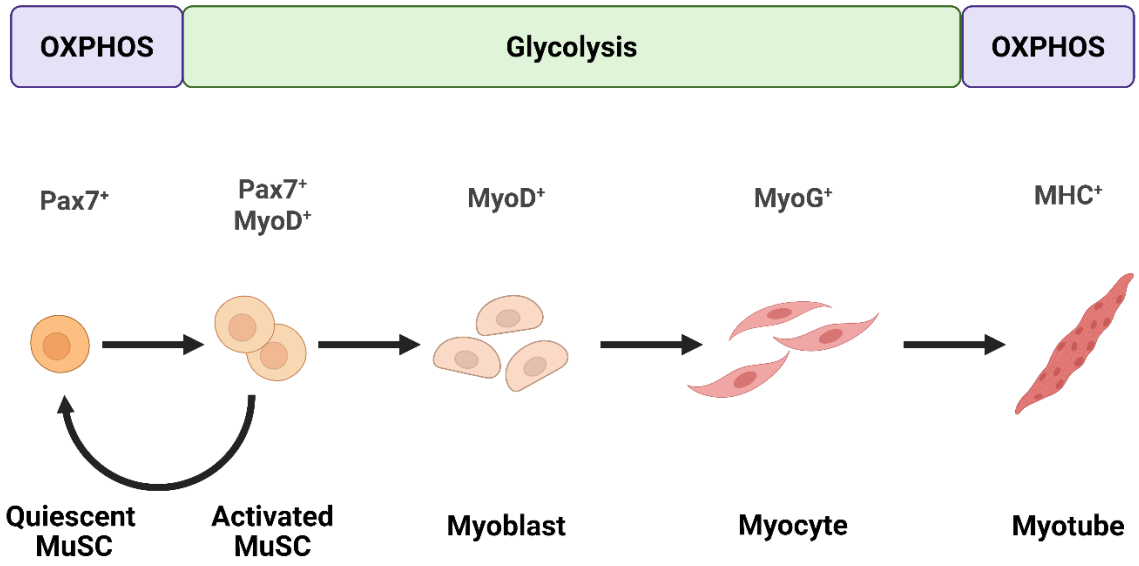

Figure 3. SKM myogenesis.
The ability of SKM to regenerate is mainly due to quiescent muscle satellite cells (MuSCs) that are activated, proliferate, and differentiate to form myotubes. Several transcription factors are expressed at different steps throughout myogenesis.

1.2 Redox homeostasis

Until recently, oxidative stress was seen as purely nefarious for cells, causing damage to DNA, lipids and proteins, with antioxidant defenses considered as protectors against oxidative damage. While this is partially true, recent evidence has shown that reactive oxygen species (ROS) are important signaling molecules especially in the activation of stem cells, and that cells strive to achieve "redox homeostasis" [24–26]. Oxidative stress is now more accurately described as a disturbance in redox homeostasis [27]. In fact, redox homeostasis is driven by redox pairs that interconvert between oxidized and reduced states including NAD^+/NADH, $NADP^+$/NADPH, and GSH/GSSG. Next, a brief overview on ROS, the antioxidant glutathione (GSH), and the crucial role of cysteine are presented.

1.2.1 Role of ROS

ROS are molecules that are generated as a normal part of aerobic metabolism, and exist primarily as superoxide anions ($O_2^{\bullet -}$), hydrogen peroxide (H_2O_2), and hydroxyl radicals ($HO^{\bullet}$) [25]. In most cell types, the main source of cellular ROS are the mitochondria, and predominantly the electron transport chain (ETC). About 0.15% of O_2 forms ROS due to premature electron flow to O_2 primarily through complexes I and III of the ETC [28].

Oxidants primarily exert their effect through the post-translational modification (PTM) of proteins, specifically by modifying thiol residues (-SH) of cysteine amino acids, leading to reversible oxidation to sulfenic acid (-SOH), which can be further oxidized to the irreversible sulfinic acid ($-SO_2H$) or sulfonic acid ($-SO_3H$) [29]. These alterations affect MuSC viability by promoting apoptosis, and affect myogenesis at the activation, proliferation, and differentiation stages. At the activation stage for example, ROS have been shown to increase

the proportion of MuSCs that undergo self-renewal [30], while at the differentiation stage, higher ROS formation results in lower mitochondrial ROS production and enhanced muscle regeneration [31]. Consistently, reductive stress, resulting from the abolition of basal ROS, has been reported to impede MuSC differentiation [32]. This highlights the dual and complex nature of ROS signaling and its impact on MuSC health.

To mitigate ROS production, and strive for redox homeostasis, cells rely on a robust antioxidant defense system.

1.2.2 Cellular antioxidant defense system

Antioxidants are substances that protect target molecules such as proteins, DNA, and lipids by delaying, preventing, or removing oxidative damage [33]. SKM-specific antioxidants can be classified as exogenous, such as vitamin C, vitamin E and trace elements, or endogenous, such as superoxide dismutase (SOD), catalase, thioredoxins, and glutathione (GSH). SOD catalyzes the dismutation of $O_2^{\bullet-}$ into H_2O_2 which is then broken down to H_2O and O_2 by catalase [19]. Thioredoxins are a family of proteins that participate in the reduction of protein disulfides and de/glutathionylation by GSH, which is a crucial low-molecular weight antioxidant that will be examined next.

1.2.3 GSH as a major cellular antioxidant

GSH is a tripeptide made of glutamate, glycine, and cysteine, and is the most abundant cellular antioxidant. It is synthesized in the cytosol by the actions of glutamate cysteine ligase (GCL) and glutathione synthetase (GSS), requiring the hydrolysis of 2 ATP molecules [34], and predominantly (~98%) exists in its reduced form (GSH), rather than its disulfide-oxidized form (GSSG) (**Figure 4**). Most cellular GSH remains in the cytosol, and about 15% is transported

to the mitochondria; however, the absolute mM concentrations are roughly equal in both spaces [35].

Given the high concentrations of GSH and GSSG in cells, this redox couple generally determines the redox state of a cell [36]. The protective function of GSH is accomplished mainly through GSH peroxidases (GPX), which reduce H_2O_2 to H_2O while oxidizing GSH to GSSG. GSH can also reversibly bind to protein cysteinyl residues (prot-SH) in a process termed glutathionylation (prot-SSG), thereby protecting these residues against irreversible oxidative damage such as sulfonylation (prot-SO_3H) [37]. In the synthesis of GSH, cysteine, which is the least abundant amino acid in cells, is the rate-limiting substrate, therefore constituting a bottleneck in this process [38].

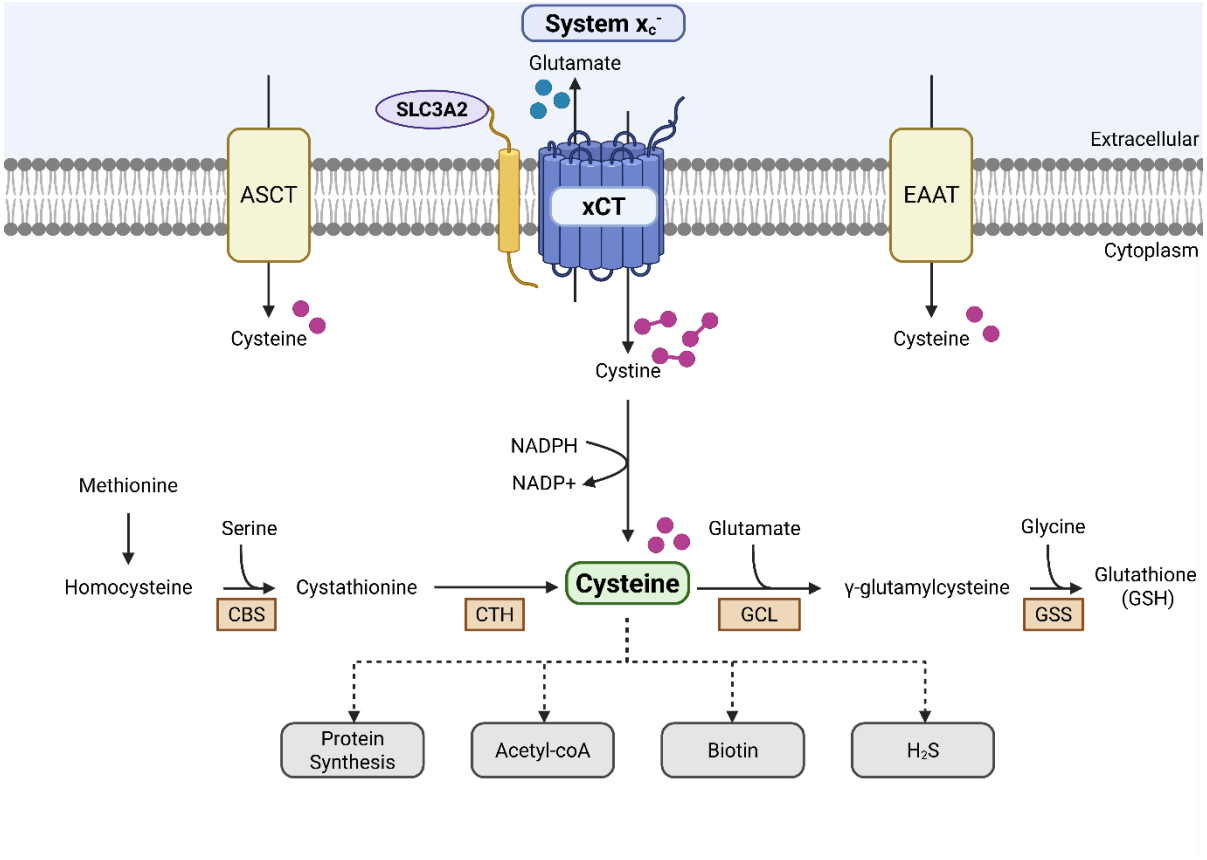

Figure 4. The import of cyst(e)ine and its role in GSH synthesis.
While cysteine can be imported via ASCT and EAAT, it is mostly present in its oxidized cystine form in the extracellular space, and is almost exclusively imported to cells via xCT. Cysteine can also be synthesized from methionine-derived homocysteine and serine. Cysteine can be used for the synthesis of GSH, proteins, and other important molecules.

1.2.4 Cyst(e)ine implications in redox homeostasis

Cysteine is a semi-essential amino acid, as it can be obtained from the diet or synthesized from the essential amino acid methionine. Cysteine has a reactive thiol (-SH) moiety, thus forming disulfide bridges within proteins and can partake in numerous PTM processes including sulfhydration, cysteinylation, glutathionylation, and nitrosylation [39], which have unpredictable and sometimes opposing effects on protein function [38,40–42].

Cysteine plays an indispensable role in redox homeostasis, being a component of the antioxidant GSH, and also a potent antioxidant by itself. As such, cells have developed multiple mechanisms to ensure a constant supply of cysteine. Cysteine can be synthesized via the reverse transsulfuration pathway (hereafter referred to as the transsulfuration pathway, TSP) through the action of cystathionine ß-synthase (CBS) which condenses serine with methionine-derived homocysteine into cystathionine, and cystathionine γ-lyase (CTH), which releases cysteine [43]. Cysteine can also be imported from the extracellular space via alanine, serine, cysteine transporters (ASCTs) or excitatory amino acid transporters (EAATs). However, since cysteine is mostly present in its oxidized cystine form in the blood, cystine is the major route of uptake through the plasma membrane, exclusively via system x_c^- (**Figure 4**).

System x_c^- is a heterodimer comprised of a heavy chain (4F2hc/SLC3A2) and a light chain (xCT/SLC7A11). The heavy chain ensures insertion in the plasma membrane while xCT is responsible for the transport activity. xCT is an antiporter that imports extracellular cystine in exchange for intracellular glutamate in a Na^+-independent but chloride-dependent manner, which is required for the transport function [44,45]. Imported cystine is rapidly reduced to cysteine by GSH or thioredoxin reductase 1 (TRR1) [46], and can then be used in the synthesis of protein and GSH, and other molecules such as coenzyme A and biotin (**Figure 4**) [38].

xCT is implicated in health and disease. Cancer cells were shown to upregulate xCT expression, which correlated with increased tumour resistance to chemotherapy drugs [47]. Similarly, inhibition of xCT by sulfasalazine in cultured breast, prostate, lung, and pancreatic cancer cells completely inhibits their growth [48], and decreases tumour metastasis *in vivo* [49]. xCT is also highly expressed in the central nervous system (CNS) [44]. In fact, $xCT^{-/-}$ mice have impaired spatial memory and increased limbic seizure susceptibility [50]. In the CNS, the implications of xCT in the manifestation of neurological disorders such as Alzheimer's diseases, Huntington's diseases, and epilepsy is related to glutamate toxicity, where glutamate accumulation in the extracellular space—either due to increased xCT activity or impairment of systems that remove glutamate—induces the formation of ROS and contributes to mitochondrial dysfunction and inflammation [51,52]. xCT inhibition also induces ferroptosis, a form a cell death that involves iron-dependent oxidative damage and uncontrolled lipid peroxidation [53].

While cystine supplementation proved effective at lowering H_2O_2-induced mitochondrial dysfunction in an SKM cell line (C2C12 myotubes) [54], the impact of xCT and dysfunctional cyst(e)ine uptake on SKM health remains poorly understood.

1.3 Aims and Hypothesis

While the connection between redox homeostasis and muscle function has been described [19], the effects of antioxidants have yielded inconsistent results in improving muscle function, hinting at the complex role of redox homeostasis in muscle health [19,55]. Therefore, a more specific understanding of the roles of cysteine and GSH in muscle metabolism and regeneration is needed to better address SKM-related pathologies. This laboratory recently

demonstrated fundamentally important implications of xCT in SKM. Specifically, dysfunctional xCT altered cellular bioenergetics throughout myogenesis and enhanced SKM differentiation [56]. However, the specific mechanistic underpinnings were not fully characterized.

To this end, this work had 3 aims:

1) Assess the impact of xCT dysfunction on GSH redox and mitochondrial bioenergetics and dynamics in proliferating MuSCs,
2) Determine the specific metabolic implications of xCT dysfunction with respect to glucose utilization and TSP activity, and
3) Determine the effect of xCT dysfunction on myogenesis.

The hypothesis was that disrupted cystine import causes defective GSH homeostasis, which drives mitochondrial fragmentation and lowers respiration, leads to increased glucose flux towards *de novo* serine synthesis, and leads to increased SKM regeneration.

Findings show perturbed GSH redox, Drp1-mediated mitochondrial fission, and higher reliance on glycolysis instead of OXPHOS as a source of ATP synthesis in xCT-mutant MuSCs. Furthermore, along with a broad metabolic reprogramming, cells diverted glucose carbons away from the TCA cycle towards *de novo* serine and cysteine synthesis in an attempt to compensate for lower GSH levels. Finally, xCT dysfunction enhanced myotube differentiation and SKM regeneration.

CHAPTER 2: MATERIALS AND METHODS

2.1 Animals

All mouse experiments were conducted according to the principles and guidelines set by the Canadian Council on Animal Care and were approved by the Animal Care Committee at the University of Ottawa. Experiments were conducted using primary muscle cells isolated from the tibialis anterior (TA) of male and female C3H/HeSnJ wild-type (WT) mice and background-matched Slc7a11$^{sut/sut}$ (xCT$^{-/-}$) mice. No sex dimorphism was observed in any outcome measured and thus experiments were conducted in pooled groups of male and female mice. Mice were housed under standard conditions, with a controlled temperature of 22-23°C, humidity levels of 30-60%, and a 12 h light/dark cycle (lights on from 07:00 to 19:00). Mice were given free access to water and fed a standard diet containing 18% protein and 6% fat (2018 Teklad Global Diet). Analyses were conducted by investigators blinded to experimental conditions.

2.2 Mouse primary muscle cell isolation and culture

Skeletal muscles of the hindlimb were rapidly dissected and cleaned from fat and connective tissue. Muscle tissues were washed with PBS supplemented with 1% antibiotic-antimycotic (Gibco). Tissues were then treated with an enzymatic cocktail containing 1 mg/ml Dispase II and 1 mg/ml Collagenase B (Sigma-Aldrich) and chopped with a sterile razor blade. The slurry was incubated at 37°C for 30 min and vortexed every 5 min during the incubation. It was then centrifuged at 500 g for 5 min and pellets were resuspended and transferred into Matrigel-coated flasks containing DMEM (25 mM glucose, Gibco) supplemented with 20% fetal bovine serum (FBS), 10% horse serum (Gibco), 2.5 ng/ml β-FGF (Sigma-Aldrich), 1x non-essential

amino acids (11140050, Gibco), and 1% antibiotic-antimycotic. Fibroblast populations were eliminated by the differential adhesion method, and primary muscle cell enrichment was achieved [57]. Primary MuSCs were cultured for 48 h. During the initial 24 h period, the cell culture medium was supplemented with 50 μM of β-mercaptoethanol (2ME), as it was required for the survival of xCT-mutant MuSCs. 2ME was removed for the remaining 24 h, except for the $Slc7a11^{sut/sut}$ + 2ME condition, which was retained as a rescue treatment.

2.3 Cell proliferation assay

IncuCyteZOOM live cell imaging system from Essen BioScience was used to assay cellular proliferation. Cells were seeded in 96-well plates (10^4 cells/well) and treated with 250 nM of the Incucyte Cytotox green dye (4633, Sartorius) with and without 2ME (50 μM). Cells were imaged for 48 h using a 10 × objective, with three to four images per well, captured every hour, and 4 technical replicates for each condition. Cell confluence was measured by phase contrast microscopy and cell death was assessed by Incucyte Cytotox dye. IncuCyteZOOM2018A software was used for automated confluence and $Incucyte^{+}$ cell measurements.

2.4 Cystine and glucose uptake in primary muscle cells

Primary MuSCs were plated at 10,000 cells per well in Matrigel-coated 96-well white/clear bottom plates. Cystine uptake was measured using a cystine uptake assay kit (UP05, Dojindo), while glucose uptake was measured using a cell-based assay kit (600470, Cayman) following manufacturers' instructions. Briefly, for cystine uptake, cells were deprived of cystine for 30 min, then incubated with the cystine analog, selenocystine at 37°C for 30 min. Cells were then incubated with fluorescein O, O'-diacrylate, and tris(2-carboxyethyl) phosphine for 30 min. For glucose uptake, cells were deprived of serum for 3 h before the assay. During the last hour,

cells were starved of glucose for 30 min, then incubated with 200 µg/ml of 2-(N-(7-nitrobenz-2-oxa-1,3-diazol-4-yl) amino)-2-deoxyglucose (2-NBDG) for 30 min. Cystine and glucose uptake rates were determined by measuring fluorescence intensity at 490/535 nm and 485/535 nm, respectively, using a BioTek Synergy H1 Multi-Mode Plate Reader (BioTek Instruments).

2.5 GSH and GSSG measurements

Primary MuSCs for each indicated condition were grown in 100 mm Petri dishes, harvested with trypsin, and then washed with ice-cold PBS. A 1:1 homogenization buffer [125 mM sucrose, 1.5 mM EDTA, 5 mM Tris, 0.5% trifluoroacetic acid (TFA), and 0.5% meta-phosphoric acid (MPA) in 50% mobile phase (10% HPLC grade methanol, 0.09% TFA – 0.2µm filtered)] was used to homogenize the cells for 20 min on ice. Cell lysates were centrifuged at 14,000 g for 20 min at 4°C, and supernatants were used for measurements. To quantify GSH and GSSG levels, an HPLC 1100 Series system (Agilent) equipped with a Pursuit C18 column (150×4.6 mm, 5 µm; Agilent) was employed with a 1 ml/min flow rate using a UV-visible wavelength detector at 215 nm (Agilent), as previously described [58]. Data were analyzed using the OpenLab CDS 2.8 software and values were normalized to cellular protein levels using a bicinchoninic acid (BCA) assay (Pierce BCA Protein Assay, 23225, Thermo Fisher Scientific).

2.6 Mitochondrial H_2O_2 emission

Mitochondrial H_2O_2 release was measured in cells using the fluorescent probe Amplex Red (ex/em: 563/587) using a Hitachi F2500 spectrophotometer as previously described [59]. Briefly, 1.5 million cells were incubated in 600 µL of buffer Z (in mM: 110 K-MES, 35 KCl, 1 EGTA, 5 K_2HPO_4, 3 $MgCl_2{\cdot}6H_2O$, and 0.5 mg/mL BSA, pH 7.3 at 4°C) in a 1 cm quartz

cuvette with magnetic stirring at 37°C supplemented with 1.2 U/mL horseradish peroxidase, and 20 μM Amplex Red. Cells were permeabilized with 2 μg/μL digitonin. After baseline readings, the following were added sequentially: 2.5-5 mM malate-glutamate, 5 mM succinate, 10 mM ADP, and 8 μM antimycin-A. Values are reported as arbitrary fluorescence units.

2.7 Cellular bioenergetics

A Seahorse XFe96 Analyzer (Agilent) was used to assess oxygen consumption rates (OCR) and extracellular acidification rates (ECAR) in primary MuSCs plated at 10,000 cells/well. Mitochondrial stress tests assessed cellular resting respiration before and following four consecutive injections: oligomycin (2 μg/mL), FCCP (2.4 μM), combined antimycin A (5.5 μM) / rotenone (7.7 μM), and monensin (20 μM). This allowed determinations of resting, leak-dependent, and maximal rates of oxygen consumption. These rates were corrected for non-mitochondrial OCR, measured as antimycin A/rotenone-independent respiration. ATP-linked OCR was calculated as the difference between resting and leak respiration, and reserve capacity was determined by subtracting resting OCR from maximal OCR. The injection of monensin at the end of the injection cycle allowed the measurement of maximal ECAR, which is a proxy measure of the glycolytic capacity of cells [60]. Beyond resting levels of glycolytic rates, glycolytic reserve was determined by subtracting resting rates from the maximal rates in the presence of monensin.

2.8 Citrate synthase activity

Maximal citrate synthase activity as a measure of mitochondrial content was determined in MuSC lysate samples in the presence of DTNB, as previously described [61]. The change in the rate of absorbance at 412 nm was measured using a Synergy Mx Microplate Reader

(BioTek Instruments). The extinction coefficient of 13.6 $mM^{-1}cm^{-1}$ was used. Values are expressed per µg cellular protein.

2.9 Cellular protein levels

To measure cellular protein content, RIPA buffer (Millipore) supplemented with a protease inhibitor cocktail (P8340, Sigma-Aldrich) and phosphatase inhibitor cocktail (78420, Thermo Fisher Scientific) was used during cell homogenization. A BCA assay (23225, Thermo Fisher Scientific) was used to measure protein concentrations, as per the manufacturer's protocol. Protein samples were kept at −80°C for later use.

2.10 Immunostaining of primary muscle cells

To conduct mitochondrial morphological analyses, cells were cultured in 8-well glass slide plates (Millipore) coated with Matrigel (Corning). Cells from different conditions were rapidly washed with 37°C PBS and then fixed with 4% PFA (Sigma-Aldrich) for 15 min. After fixation, cells were washed twice with PBS and incubated for 2 h at room temperature (RT) in PBS containing 1% BSA, 0.2% Triton-X (Sigma-Aldrich), and anti-TOMM20 (1:500, 11802, Protein Tech). Cells were washed twice with PBS and incubated for 1 h at RT in PBS containing 1% BSA and a secondary antibody (Alexa Fluor 488 goat anti-rabbit IgG (H+L), 1:500, A-11008, Thermo Fisher Scientific). After 2 washes, cells were incubated for 5 min at RT with 4,6-diamidino-2-phenylindole (DAPI, 1:1000, Sigma-Aldrich). The polypropylene wells were removed from the slide before mounting the cells in ProLong Gold antifade reagent (Invitrogen). Cells were imaged using a confocal microscope (Zeiss LSM880) equipped with an AiryScan FAST technology 63X/1.4 oil objective. Mitochondrial morphological analyses

were performed using Mitochondria Analyzer, a three-dimensional mitochondrial analysis pipeline in ImageJ/Fiji [62].

2.11 Western blot analyses

Cell lysate samples were prepared in 1 x Laemmli buffer containing 100 mM DTT. Samples were separated on SDS-PAGE and then transferred onto PVDF (Bio-Rad) or nitrocellulose membranes. For glutathionylation, MFN1/2 oligomerization, and DRP1 oligomerization immunoblots, samples were prepared in 1 x Laemmli without DTT. Membranes were blocked with 5% BSA in Tris-buffered saline containing 0.1% Tween-20 (TBST) for 1 h at RT. Primary antibody incubations were overnight at 4°C. The following antibodies were purchased from Abcam: GPX1 (1:2000, ab22604), GPX4 (1:2000, ab16800), Total OXPHOS (1:1000, ab110413), and MFN1/2 (1:5000, ab57602). Antibodies from Santa Cruz were: GCL-c (1:1000, sc-390811), and GSS (1:1000, sc-365863). Antibodies from Protein Tech were: GCL-m (1:1000, 14241-1), OPA1 (1:2000, 27733-1), PHGDH (1:2000, 14719-1), PSAT1 (1:5000, 10501-1), PSPH (1:2000, 14513-1), CBS (1:2000, 14787-1), CTH (1:2000, 12217-1), GS (1:2000, 11037-2). Additional antibodies included: Glutathione (1:1000, 101-A, Virogen), and DRP1 (1:2000, 611113, BD Biosciences). Primary antibodies used against loading controls were: GAPDH (1:10000, 60004-1-Ig, Proteintech), and Vinculin (1:5000, ab129002, Abcam). A ChemiDoc™ MP Imaging System (Bio-Rad) was used to visualize protein bands and ImageJ software was employed to conduct protein band densitometry. The abundance of all target proteins is presented as normalized to the indicated loading control.

2.12 Metabolomic stable isotope tracer analysis (SITA) and LC-MS

Stable isotope tracing was performed as previously described [63]. Briefly, cells were seeded in 60 mm dishes to achieve ~75% confluency for 24 h. DMEM was then replaced with equivalent media without 2ME, FBS, and horse serum, supplemented with 20% dialyzed FBS for 24 h. Then, an equivalent volume of labelled medium with 25 mM [U-^{13}C]-glucose (CLM-1396-1, Cambridge Isotope Laboratories Inc) was added for the indicated time points. Cells were washed three times with ice-cold 150 mM ammonium formate solution, quenched in 230 µL ice-cold LC/MS grade 1:1 methanol:water solution, and vortexed for 10 s, before adding 220 µL acetonitrile. The collected cells were then homogenized using a bead mill homogenizer at 4°C for two rounds of 60 s at 30 Hz (Fisherbrand Bead Mill 24 Homogenizer). Homogenates were incubated with a 2:1 dichloromethane:water solution on ice for 10 min then centrifuged at 1,500 g for 10 min at 1°C. Water-soluble metabolites were collected from the upper phase, dried using a refrigerated CentriVap Vacuum Concentrator at −4°C (LabConco Corporation), and stored at -80°C before LC-MS analyses. Control samples that were not incubated with [U-^{13}C]-glucose were included in all tracer experiments.

Samples were randomized and re-suspended with 75% acetonitrile, cleared by centrifugation, and run in negative ESI on a 6545B Q-TOF mass spectrometer (Agilent) equipped with a 1290 Infinity II ultra-high-performance LC (Agilent) using hydrophilic interaction chromatography (HILIC-Z). Continuous internal mass calibration was executed using signals from purine [12,000 full width at half maximum (FWHM) resolution] and hexakis (1H, 1H, 3H-tetrafluoropropoxy) phosphazine (24,000 FWHM resolution). HILIC separation was obtained using the Poroshell 120 HILIC-Z column (2.1; 100 mm, 2.7 mm; Agilent) and the

corresponding guard column. The chromatographic conditions and mass spectrometry acquisition parameters are described elsewhere [64]. The binary solvent system consisted of 10 mM ammonium acetate (pH 9) in water (solvent A) and 100 mM ammonium acetate in 85% acetonitrile (solvent B), both having 0.1% medronic acid. The gradient for separation started at 96% B for 1.5 min, then decreased from 96% to 65% B for 6.5 min followed by a 2 min hold at 65% B, and 7 min of re-equilibration to 96% B. This took the total run time to 17 min at a 0.25 mL/min flow rate. The injection volume was 10 µL, and the column temperature was maintained at 35°C.

Mass spectrometry detection was performed in negative ESI full scan mode with a mass range of 50 to 1000 m/z. The mass spectrometer source conditions consisted of a capillary voltage of 3000 V. Drying and sheath gas temperatures were set to 200°C and 300°C and flow rates were set to 10 and 12 L/min, respectively. Nebulizer pressure was set to 40 psi and the fragmentor voltage was 175 V. Data were acquired in centroid mode at the rate of 3 spectra per second in the extended dynamic range mode (2 GHz). A target list of metabolites was created using "MassHunter Pathways to PCDL" software (Agilent). Metabolite retention times were provided from an in-house database.

2.13 Metabolomic profiling

Samples were collected and run using LC-MS as mentioned in the SITA protocol but without tracer. All values were normalized to the protein content of parallel plates. Data were analyzed using Python (Python Software Foundation. Python Language Reference, version 3.8.18. Available at www.python.org) and R (version 4.2.2.) [65]. All figures were produced using the matplotlib [66] and ggplot2 [67] libraries. Unless stated otherwise, statistical tests were

performed through their respective Scipy method [68]. All data and code for these analyses are available in the GitHub repository: https://github.com/lkenn012/xCT_metabolomics

2.14 Analysis of metabolomic profiling data

Hierarchical clustering and several statistical methods were applied after pre-processing the data from sample groups. Three different feature selection methods were employed for differential metabolite determination including Welch's t-test; orthogonal partial least squares discriminant analysis (OPLS-DA); and significance analysis of microarrays (SAM). Missing values were imputed according to a limit of detection imputation defined as ⅕ of the minimum value per metabolite feature. Following this, abundance values were $\log_{10}$-transformed and z-score normalized. Z-score normalized values were used for all statistical analyses except for significance testing by Welch's t-test, where the raw values including missing values were used.

Enrichment plots for metabolite clusters were generated using the Metaboanalyst web server [69] via over-representation analysis, using all identified metabolites in the dataset as background (excluding non-specific metabolites such as total hexoses). Agglomerative hierarchical clustering linkages were determined according to the Ward algorithm applied to Euclidean distances (maximum cluster distance of 4) for Slc7a11$^{sut/sut}$ and WT unlabelled metabolomics data. Robinson-Fould metrics were computed using the ETE3 Python library [70] (ete3 version 3.1.3); these metrics estimate the conservation between two clustering dendrograms based on the proportion of shared linkages between metabolites.

2.15 Immunostaining of MuSC myogenic markers

Cells cultured in Matrigel-coated dishes were harvested 24 h after plating (myoblasts) and 24 h after differentiation. 100,000 cells (in 100 µl) were loaded into a double Cytofunnel (Thermo Fisher Scientific) set on a double Cytoslide (Thermo Fisher Scientific) and centrifuged at 500 rpm for 5 min at RT using a cytocentrifuge (Epredia™ Cytospin™ 4). Cells were fixed with 4 % paraformaldehyde (PFA, Sigma) for 3 min and quenched with 100 mM glycine (Biobasic) for 5 min at RT. Cells were washed 3 times with 1 x PBS before staining. Cells were then permeabilized for 10 min in PBS containing 0.2 % Triton-X (Sigma), blocked in 5 % goat serum (Sigma), and 2 % BSA-PBS for 30 min, and then incubated for 2 h with Pax7 (1:2 Pax7, DSHB) at RT. The following day, sections were washed three times with PBS and incubated in species-specific fluorescent secondary antibodies diluted in PBS containing 4,6-diamidino-2-phenylindole (DAPI). Cells were washed, then incubated for 1 h with the secondary antibody Alexa Fluor 568 Goat anti-Mouse IgG1 (1:2000, A-21124, Thermo Fischer Scientific) diluted in 1x PBS containing DAPI at RT. To assess the S-phase entry, cells were incubated with 1 µM of 5-ethynyl-2′-deoxyuridine (EdU, Lumiprobe) for 24 h prior to harvesting. A 30-min incubation with the labeling mix [0.1 µM Sulfo-Cyanine5 azide dye (Lumiprobe), 2 mM copper (II) sulfate pentahydrate (Sigma), and 20 mg/ml of l-ascorbic acid (Sigma)] were applied before blocking.

For assessment of differentiation, cells were cultured in 24-well plates and differentiated for the following intervals: 1 day, 2 days, and 4 days. At each time point cells were fixed with 4 % PFA (Sigma) for 15 min after 3 washes in PBS. Cells were permeabilized for 15 min in PBS containing 0.5 % Triton-X and incubated with myosin (1:50, DSHB, MYH1E) overnight at 4 °C. Cells were washed in PBS and then incubated for 1 h with species-specific secondary

antibodies diluted in 1 x PBS containing DAPI at RT. Wells were filled with PBS and cells were imaged at 10x on a Zeiss AxioObserver Z1 fluorescent microscope equipped with an AxioCam MRm CCD camera.

2.16 Muscle injury

Subcutaneous injections of buprenorphine (0.1 mg/kg) were administered 30 min prior to cardiotoxin treatment. Mice were anesthetized with isoflurane, hindlimbs were disinfected with ethanol and the left tibialis anterior (TA) muscle was injected with 50 µl cardiotoxin (10 µM, L8102, Latoxan). Tissues were collected at 21 days post-injury.

2.17 Muscle cross-sectional area determinations

To measure the cross-sectional area (CSA) of myofibers, transverse 14 µm cryosections were stained with hematoxylin and eosin (H&E). Samples were imaged at 20x using an EVOS FL Auto 2 microscope (Thermo Fisher Scientific) and analyzed using Cellpose [71] and ImageJ.

2.18 Statistics

Unless otherwise mentioned, all data are shown as a mean ± standard error of the mean (SEM). Statistical analyses were conducted using Prism (GraphPad, La Jolla, CA). A two-tailed Student's t-test was used to determine statistical significance between WT vs. Slc7a11$^{sut/sut}$. The statistical significance of primary MuSCs experiments with 3 different conditions (WT, Slc7a11$^{sut/sut}$, and Slc7a11$^{sut/sut}$ + 2ME) was determined using one-way ANOVA with Tukey post hoc tests. P-values < 0.05 were considered statistically significant.

CHAPTER 3: RESULTS

3.1 Disrupted cystine import alters GSH redox and mitochondrial bioenergetics and dynamics.

3.1.1 xCT dysfunction perturbs GSH homeostasis

To study how xCT dysfunction impacts MuSC proliferation and metabolism, MuSCs were isolated from Slc7a11$^{sut/sut}$ and background matched WT mice. Slc7a11$^{sut/sut}$ mice have a spontaneous deletion in the xCT-encoding *Slc7a11* gene spanning from intron 11 through exon 12, resulting in the truncation of the xCT protein at the C terminus [72,73]. Slc7a11$^{sut/sut}$ cells had low viability without β-mercaptoethanol (2ME) supplementation (**Figure 5A**). 2ME, a potent reducing agent, reduces extracellular cystine to cysteine, thus bypassing xCT and allowing the uptake of cysteine via ASCTs and EAATs. Therefore, xCT dysfunction had profound impacts on MuSC proliferation. To this end, to support proliferation in subsequent experiments, MuSCs were cultured in the presence of 2ME, which was removed 24 hr before experimental analyses to unmask the impacts of xCT deficiency on metabolism.

To assess the extent of xCT dysfunction, cellular cystine uptake was measured in MuSCs. Cystine uptake was 52% lower in Slc7a11$^{sut/sut}$ compared to WT (**Figure 5B**). Similarly, WT cells treated with the xCT inhibitor erastin (10 μM) exhibited a 50% decrease in cellular cystine uptake. In line with impaired cystine uptake, HPLC measurements demonstrated lower intracellular levels of GSH, GSH:GSSG, and total GSH, but higher GSSG in Slc7a11$^{sut/sut}$ MuSCs compared to WT (**Figure 5C**). Slc7a11$^{sut/sut}$ MuSCs that were supplemented with 2ME had partially restored GSH and GSSG levels, comparable with WT MuSCs. Furthermore, immunoblotting analysis revealed a trend for lower protein glutathionylation levels in Slc7a11$^{sut/sut}$ MuSCs compared to WT (**Figure 6A**).

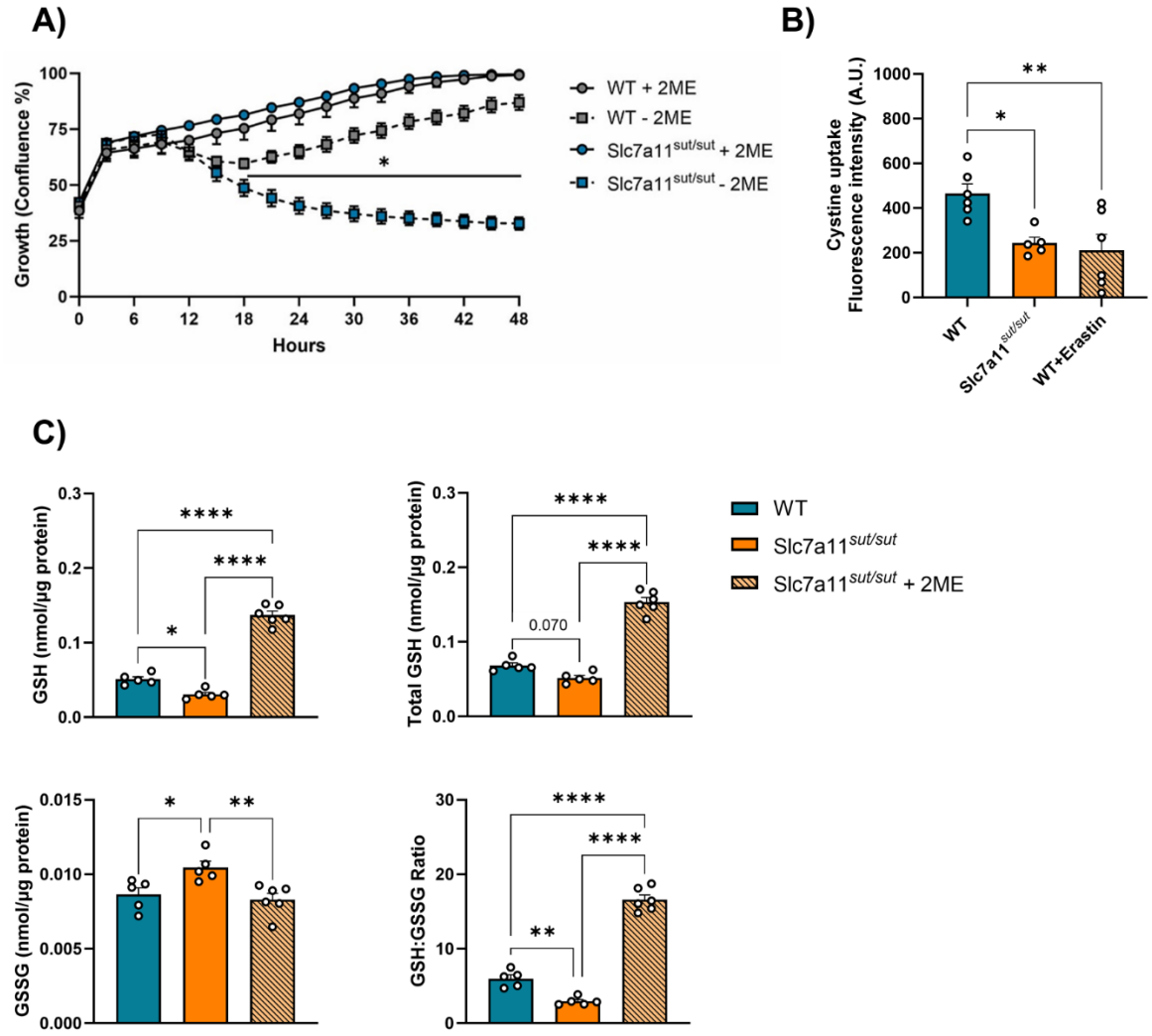

Figure 5. Impact of xCT dysfunction on MuSC proliferation, cystine uptake, and GSH. **(A)** Real-time measurement of primary myoblast confluence using an Incucyte live cell imager. **(B)** Rate of cystine uptake measured using the fluorescent probe fluorescein O, O'-diacrylate in WT, Slc7a11$^{sut/sut}$, and WT + erastin MuSCs. **(C)** Reduced glutathione (GSH), oxidized glutathione (GSSG), GSH:GSSG ratio, and total glutathione (GSH + (2 x GSSG)) measured by HPLC in WT, Slc7a11$^{sut/sut}$, and Slc7a11$^{sut/sut}$ + 2ME. Comparisons between groups were determined using a two-way ANOVA with Tukey post-hoc tests, n = 6 (A); one-way ANOVA with post hoc Tukey HSD test, n = 5-6 (B-C). Results are presented as mean ± SEM, *p < 0.05, **p < 0.01, ***p < 0.001, ****p < 0.0001.

To evaluate the impact of xCT deficiency on mechanisms of GSH biosynthesis, protein levels of key enzymes involved in GSH synthesis were measured, namely glutamate-cysteine ligase catalytic (GCL-c) and modifier (GCL-m) subunits and GSH synthetase (GSS). Immunoblotting analyses showed similar levels of GCL-c, but lower levels of GCL-m in Slc7a11$^{sut/sut}$ MuSCs compared to WT (**Figure 6B**). Conversely, GSS levels, which catalyzes the last step of GSH synthesis by adding glycine, were higher in Slc7a11$^{sut/sut}$ MuSCs compared to WT, potentially in a failed attempt to compensate for decreased cysteine availability for GSH synthesis. Finally, H_2O_2 production was measured to determine whether altered cellular GSH redox affected the susceptibility of Slc7a11$^{sut/sut}$ MuSCs to oxidative stress. Across various mitochondrial respiratory states, Slc7a11$^{sut/sut}$ MuSCs exhibited higher H_2O_2 levels compared to WT cells (**Figure 6C**). Notably, protein levels of GSH peroxidase 1 (GPX1) and 4 (GPX4) remained comparable between WT and Slc7a11$^{sut/sut}$ MuSCs (**Figure 6D**), suggesting that increased H_2O_2 levels are likely not due to lower protein levels of GSH-dependent antioxidant enzymes, but rather may reflect a limited GSH availability. Collectively, these findings indicate that the xCT mutation disrupts intracellular GSH levels, likely due to impaired cystine influx and thus GSH synthesis.

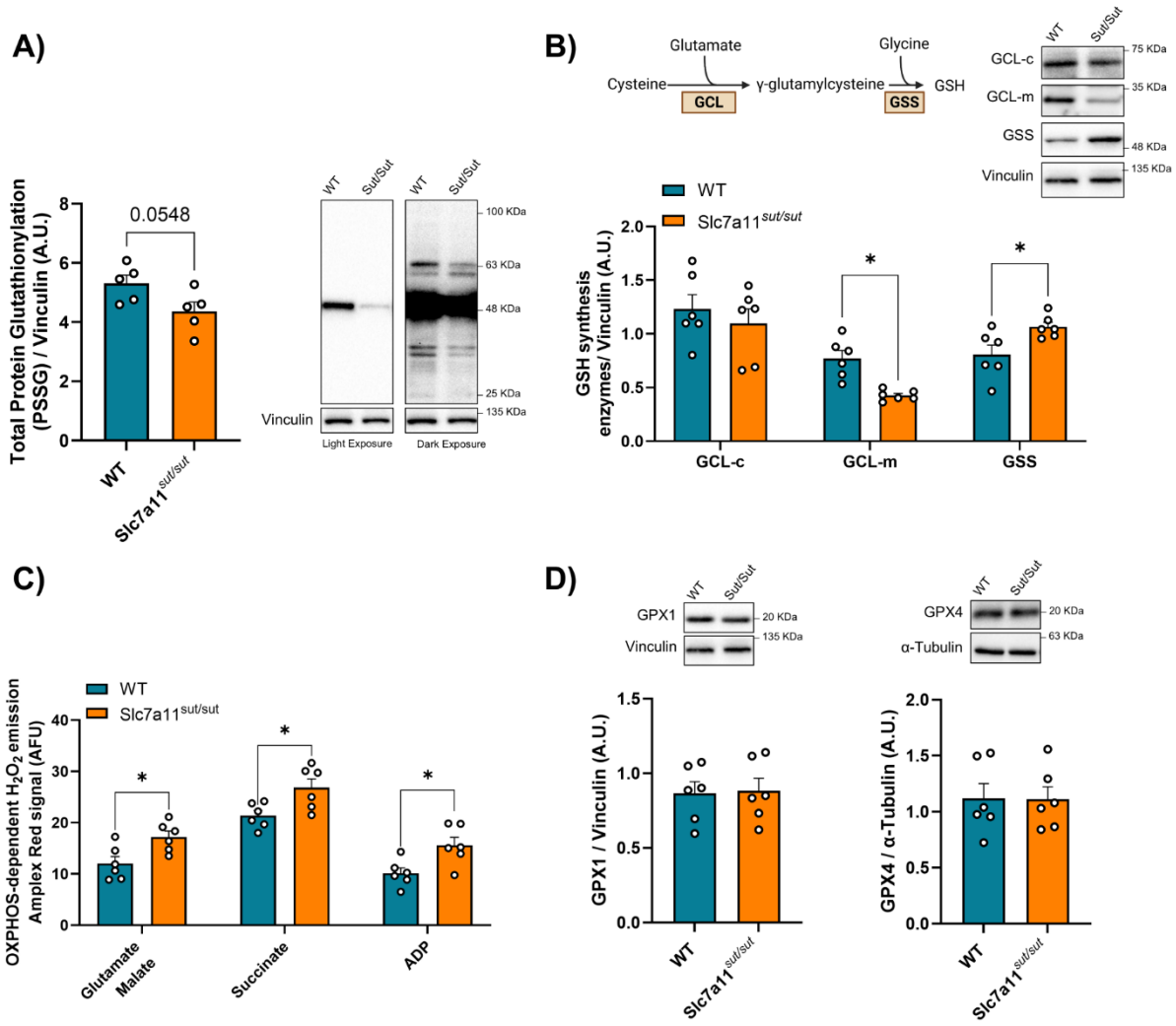

Figure 6. xCT controls GSH synthesis and OXPHOS-dependent H_2O_2 release in proliferating MuSCs.

(A-B) Immunoblots of WT and Slc7a11$^{sut/sut}$ MuSCs against **(A)** post-translational glutathionylation, and **(B)** GSH synthesis enzymes, glutamate-cysteine ligase (GCL) catalytic (GCL-c) and modifier (GCL-m) subunits, and GSH synthetase (GSS). **(C)** Mitochondrial H_2O_2 emissions in digitonin permeabilized WT and Slc7a11$^{sut/sut}$ MuSCs. **(D)** Immunoblots of WT and Slc7a11$^{sut/sut}$ MuSCs against GPX1 and GPX4. Comparisons between groups were determined using a two-tailed Student's t-test, n = 5-6. Results are presented as mean ± SEM, *$p < 0.05$.

3.1.2 xCT dysfunction decreases mitochondrial oxidative capacity

Mitochondrial metabolism is of central importance to SKM health. Given that metabolic processes are redox-sensitive [74], the next aim was to assess mitochondrial respiration and glycolytic flux using Seahorse XF analyses in WT and Slc7a11$^{sut/sut}$ MuSCs. Slc7a11$^{sut/sut}$ MuSCs displayed overall lower oxidative capacity with a 42% decrease in resting, a 33% decrease in leak, and a 50% decrease in maximal oxygen consumption rates (OCR) compared to WT MuSCs (**Figure 7A)**. Quantification of extracellular acidification rates (ECAR), a proxy measure of glycolysis, revealed that Slc7a11$^{sut/sut}$ MuSCs display a trend for a decrease in resting and maximal ECAR rates compared to WT MuSCs (**Figure 7B**). However, when using the Mookerjee method [75] to evaluate absolute levels of ATP production from glycolysis and OXPHOS under different metabolic states, it was clear that Slc7a11$^{sut/sut}$ MuSCs were more dependent on glycolysis than OXPHOS for ATP production. Specifically, there was a higher proportion of ATP derived from glycolysis in Slc7a11$^{sut/sut}$ MuSCs during resting (**Figure 7C**) and maximal (**Figure 7D**) respiration states. In line with these findings, glucose uptake was higher in Slc7a11$^{sut/sut}$ than in WT MuSCs, further demonstrating the higher overall requirements for glucose in xCT-deficient cells (**Figure 7E**).

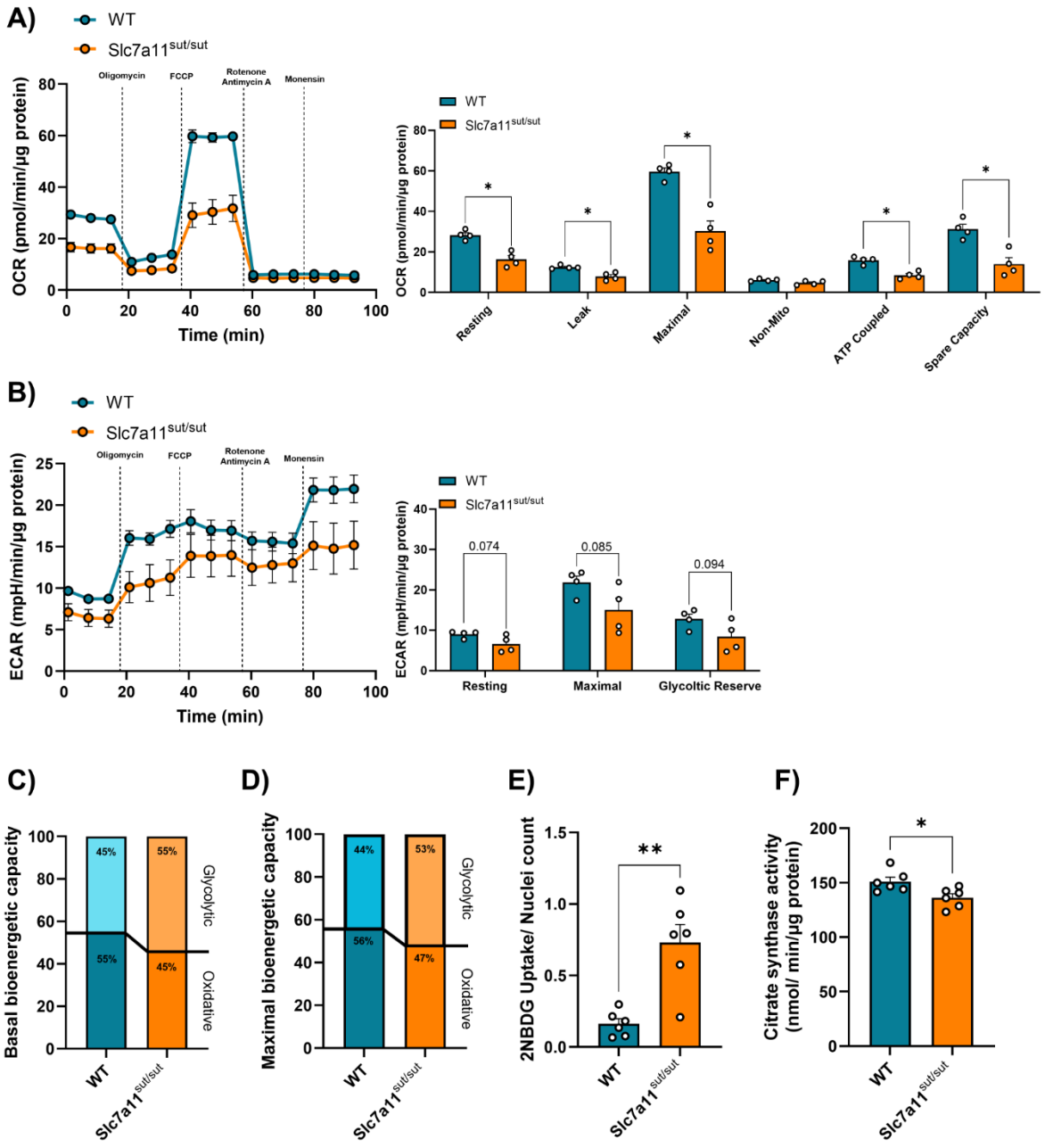

Figure 7. xCT dysfunction leads to impaired cellular bioenergetics.
(A) Oxygen consumption rates (OCR) and **(B)** extracellular acidification rates (ECAR) measured in primary WT and Slc7a11$^{sut/sut}$ MuSCs. The contributions of OXPHOS and glycolysis to ATP production were calculated following the Mookerjee *et al*., 2017 method for **(C)** Basal and **(D)** Maximal bioenergetic capacities in WT and Slc7a11$^{sut/sut}$ MuSCs. **(E)** Glucose uptake quantified using 2-NBDG in WT and Slc7a11$^{sut/sut}$ primary MuSCs. **(F)** Citrate synthase enzyme activity in WT and Slc7a11$^{sut/sut}$ MuSCs. The statistical significance of the differences between groups was determined using a two-tailed Student's t-test, n = 4 (A-D); n = 6 (E-F). Results are presented as mean ± SEM, *p < 0.05, **p < 0.01.

To determine whether the diminished OXPHOS capacity observed in Slc7a11$^{sut/sut}$ MuSCs resulted from decreased mitochondrial content, citrate synthase activity and the protein levels of key OXPHOS proteins were measured. Findings showed that citrate synthase activity (**Figure 7F**) and protein levels of OXPHOS complexes I, II, and IV (**Figure 8**) were lower in Slc7a11$^{sut/sut}$ compared to WT MuSCs, indicative of decreased mitochondrial content in Slc7a11$^{sut/sut}$ compared to WT MuSCs. Overall, findings are consistent with the conclusion of diminished mitochondrial oxidative capacity in Slc7a11$^{sut/sut}$ MuSCs.

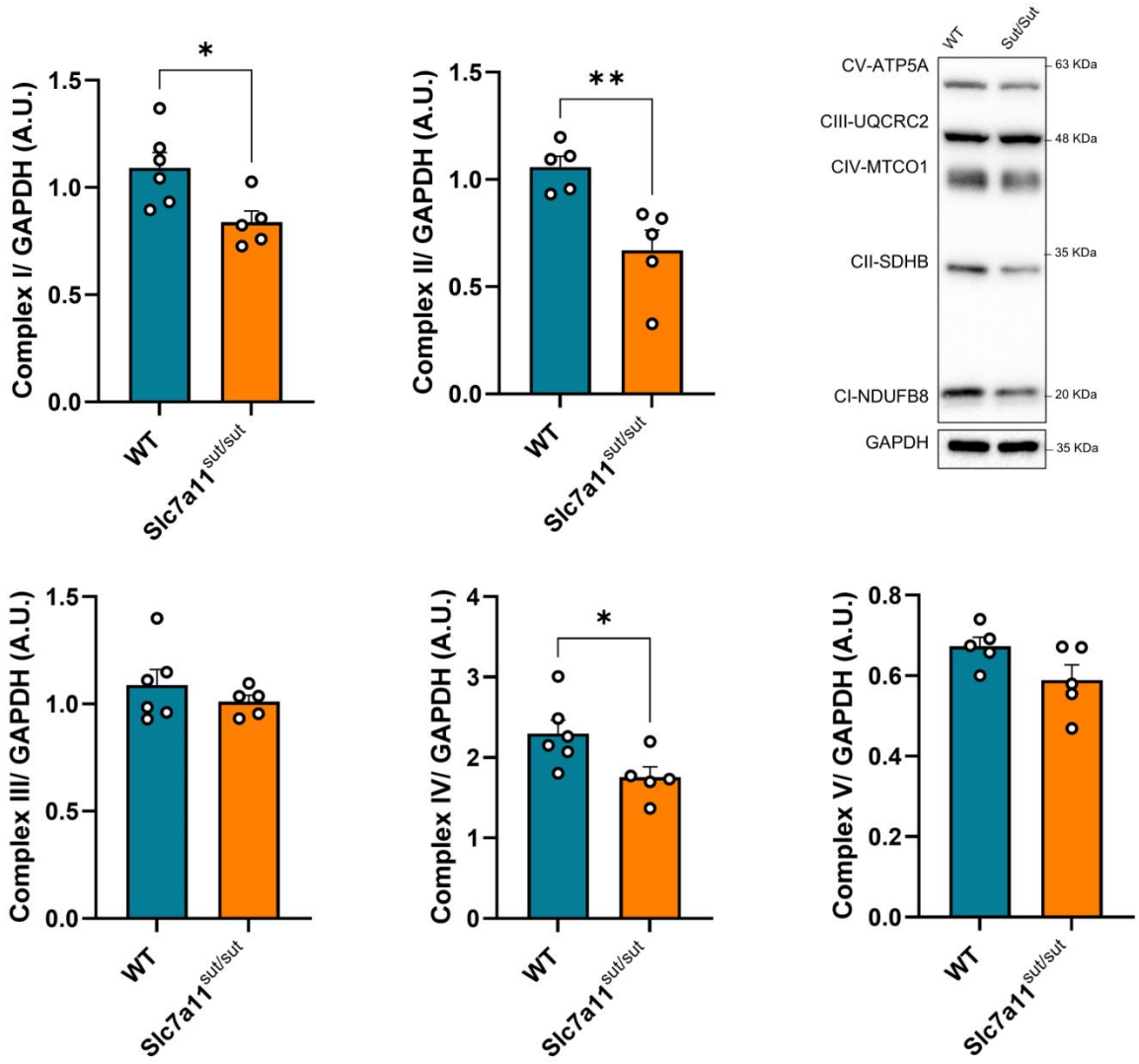

Figure 8. Lower abundance of mitochondrial OXPHOS complexes in Slc7a11$^{sut/sut}$ MuSCs.

Immunoblots of mitochondrial OXPHOS complexes in WT and Slc7a11$^{sut/sut}$ MuSCs. The statistical significance of the differences between groups was determined using a two-tailed Student's t-test, n = 5-6. Results are presented as mean ± SEM, *p < 0.05, **p < 0.01.

3.1.3 xCT dysfunction leads to Drp1-mediated mitochondrial fission

The dynamic network structure of mitochondria is redox sensitive and alters mitochondrial bioenergetics and metabolism. The next aim was thus to investigate how xCT dysfunction affects mitochondrial structure by staining for TOMM20, a ubiquitous mitochondrial outer membrane protein. Quantitative analysis of TOMM20-stained MuSCs revealed that the mitochondrial network was more fragmented in Slc7a11$^{sut/sut}$ MuSCs compared to WT MuSCs, as indicated by the lower total branch length per mitochondrion and lower number of branches per mitochondrion (**Figure 9A, B, and C**). The fragmented mitochondrial reticulum observed in Slc7a11$^{sut/sut}$ MuSCs was not attributed to differences in protein levels of the large GTPase proteins that maintain mitochondrial fusion, including OPA1, and MFN1/2. Moreover, levels of the fission protein DRP1 were comparable between Slc7a11$^{sut/sut}$ MuSCs and WT (**Figure 9D**). As GSH redox also plays a role in determining MFN1/2 oligomerization [76,77], immunoblots under non-reducing conditions were performed to preserve disulfide bonds. Slc7a11$^{sut/sut}$ MuSCs had less MFN1/2 oligomers (between 160 and 250 kDa, **Figure 10A**) compared to WT MuSCs, but displayed higher DRP1 oligomerization compared to WT MuSCs (**Figure 10B**). In summary, xCT deficiency results in a fragmented mitochondrial network in MuSCs associated with lower MFN1/2 oligomers and higher DRP1 oligomerization, which may contribute to impaired mitochondrial oxidative capacity.

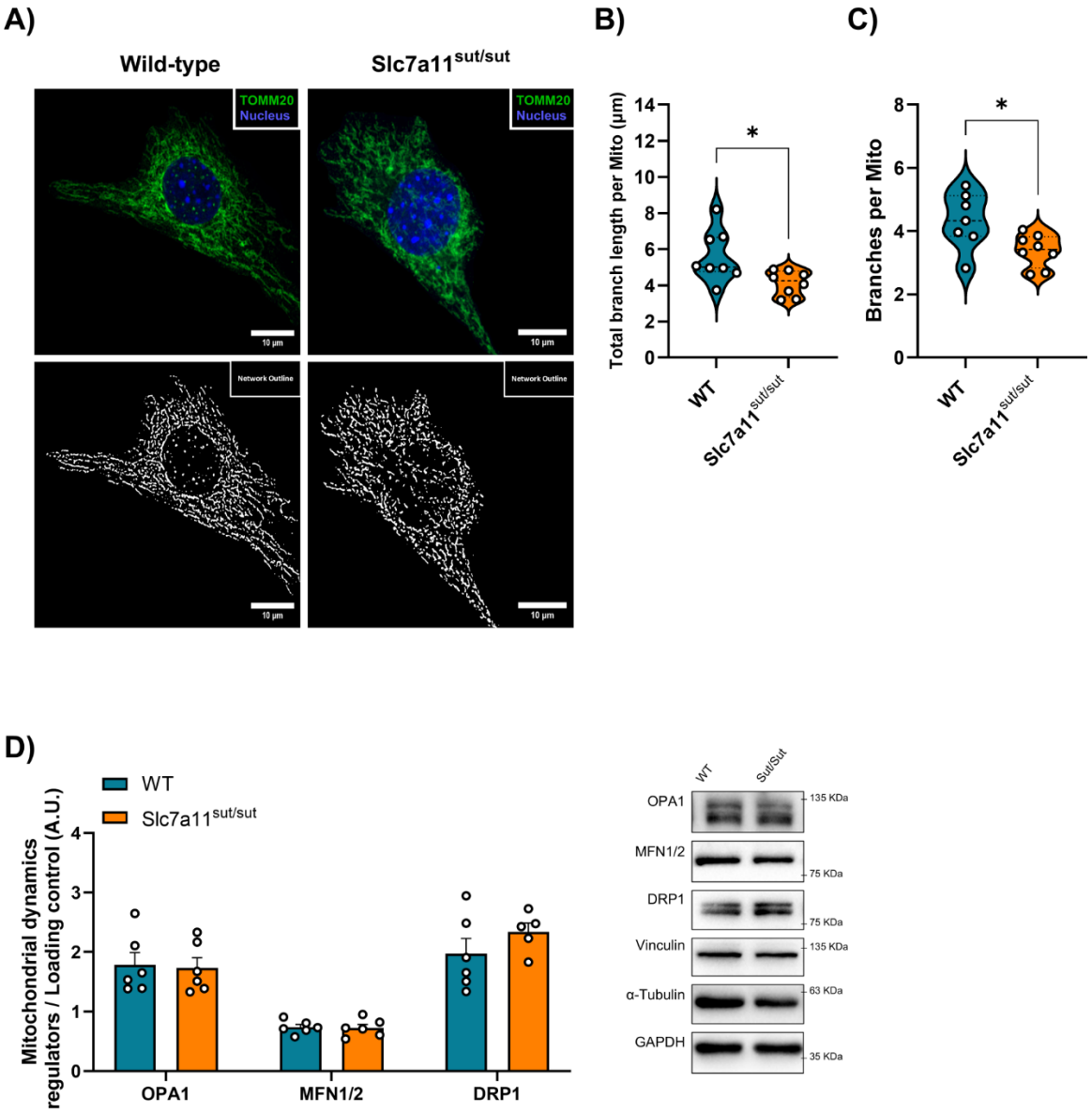

Figure 9. xCT dysfunction leads to fragmented mitochondria but no changes in the abundance of mitochondrial dynamics proteins.

(A) Immunofluorescence staining of TOMM20 (green) and DAPI (blue), scale bar = 10 µm. Thresholded TOMM20 signals are shown in white. **(B-C)** Quantitative morphometric analyses of TOMM20-staining examining **(B)** total branch length per mitochondria (µm), and **(C)** number of branches per mitochondria. Each data point represents a region of interest (ROI) containing 2 to 3 mitochondria. 2 ROI were imaged and analyzed for each sample, n = 4. **(D)** Immunoblots of mitochondrial dynamics proteins in WT and Slc7a11$^{sut/sut}$ MuSCs. The statistical significance of the differences between groups was determined using a two-tailed Student's t-test, n = 4 (A-C); n = 5-6 (D). Results are presented as mean ± SEM, *p < 0.05.

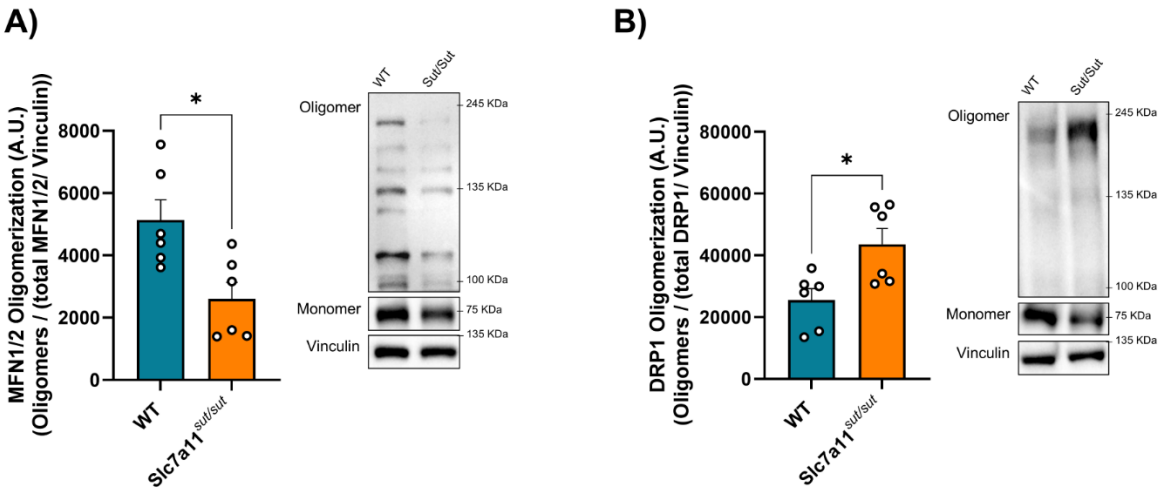

Figure 10. Altered oligomerization of mitochondrial dynamics proteins in Slc7a11$^{sut/sut}$ MuSCs.

(A-B) Immunoblots of **(A)** MFN1/2 oligomerization, and **(B)** DRP1 oligomerization in primary WT and Slc7a11$^{sut/sut}$ MuSCs. The statistical significance of the differences between groups was determined using a two-tailed Student's t-test, n = 6. Results are presented as mean ± SEM, *p < 0.05.

3.2 Disrupted cystine import leads to metabolic reprogramming characterized by increased transsulfuration pathway activity.

3.2.1 Global metabolic alterations in Slc7a11$^{sut/sut}$ MuSCs

To elucidate the specific metabolic pathways impacted by impaired xCT function, the global metabolite profiles of WT and Slc7a11$^{sut/sut}$ MuSCs under steady-state conditions were analyzed using ion-pairing LC-MS. Slc7a11$^{sut/sut}$ MuSCs had lower levels of GSH, 4,5-dihydroorotate, uracil, dihydrouracil, and orotic acid, but higher levels of several amino acids compared to WT MuSCs, including proline, methionine, glycine, glutamine, and branched-chain amino acids (BCAAs, valine, leucine, and isoleucine) (**Figure 11A**). Metabolite set enrichment analyses of the 27 differing metabolites further highlighted major differences between Slc7a11$^{sut/sut}$ and WT MuSCs in the metabolism of BCAAs, pyrimidines, cysteine, methionine, and GSH (**Figure 11B**). As anticipated, metabolites involved in endogenous cysteine biosynthesis, such as serine and methionine, were more abundant in Slc7a11$^{sut/sut}$ MuSCs compared to WT (**Figure 11C**).

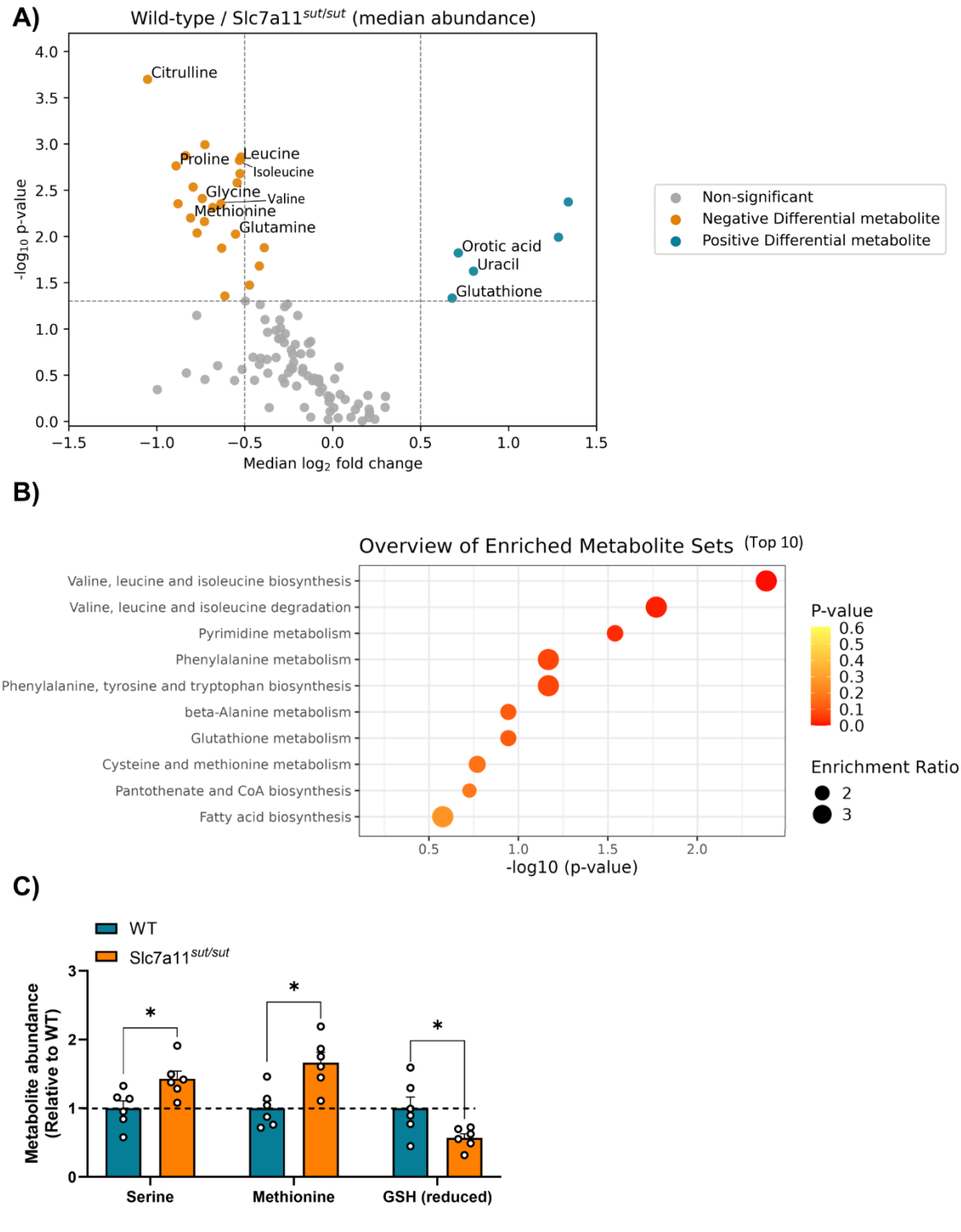
A)
Wild-type / Slc7a11sut/sut (median abundance)
Citrulline
Proline
Leucine
Isoleucine
Glycine
Valine
Methionine
Glutamine
Orotic acid
Uracil
Glutathione
-log10 p-value
Median log2 fold change
Non-significant
Negative Differential metabolite
Positive Differential metabolite
B)
Overview of Enriched Metabolite Sets (Top 10)
Valine, leucine and isoleucine biosynthesis
Valine, leucine and isoleucine degradation
Pyrimidine metabolism
Phenylalanine metabolism
Phenylalanine, tyrosine and tryptophan biosynthesis
beta-Alanine metabolism
Glutathione metabolism
Cysteine and methionine metabolism
Pantothenate and CoA biosynthesis
Fatty acid biosynthesis
-log10 (p-value)
P-value
Enrichment Ratio
C)
WT
Slc7a11sut/sut
Metabolite abundance (Relative to WT)
Serine
Methionine
GSH (reduced)

Figure 11. Distinct metabolomic profiles in Slc7a11$^{sut/sut}$ MuSCs.
(A) Volcano plot of metabolite profiles. **(B)** KEGG metabolite set enrichment analysis (top 10, p-value < 0.30) of metabolic pathways altered in Slc7a11$^{sut/sut}$ MuSCs. **(C)** Abundance of serine, methionine, and GSH (reduced) (relative to WT). Comparisons between groups were determined using a two-tailed Student's t-test, n = 6 (C). Results are presented as mean ± SEM, *p < 0.05.

3.2.2 Lower entry of glucose carbons into the TCA cycle in Slc7a11$^{sut/sut}$ MuSCs

Given the evidence of increased need for glucose in Slc7a11$^{sut/sut}$ MuSCs, stable isotope tracing analysis (SITA) of [U-^{13}C]-glucose was performed to elucidate alterations in glucose flux through specific metabolic pathways. After testing various incubation times following standard practices [78], a 12-hour incubation with ^{13}C-labelled glucose proved optimal to detect flux through most metabolic pathways of interest. The integration of ^{13}C into the glycolytic metabolites 3-phosphoglycerate (3PG) and 2-phosphoglycerate (2PG) was similar between Slc7a11$^{sut/sut}$ and WT MuSCs (**Figure 12A and B**). Glucose-derived pyruvate is the major end-product of glycolysis, which can subsequently be converted to acetyl-CoA by pyruvate dehydrogenase (PDH) to enter the TCA cycle and give rise to citrate m+2 (in green, **Figure 12A**), or can contribute to TCA cycle anaplerosis via pyruvate carboxylase (PC) production of oxaloacetate, giving rise to citrate m+3 (in purple, **Figure 12A**). Slc7a11$^{sut/sut}$ MuSCs displayed trends for elevated amounts of pyruvate m+3 and lactate m+3 compared to WT (**Figures 12C**) indicating that pyruvate accumulates instead of entering the TCA cycle. Indeed, the calculated citrate m+2 / pyruvate m+3 and citrate m+3 / pyruvate m+3 ratios, proxy measures for PDH- and PC-dependent labelling respectively [79], were lower in Slc7a11$^{sut/sut}$ MuSCs (**Figure 12D**). Moreover, Slc7a11$^{sut/sut}$ MuSCs had a lower carbon labelling to TCA cycle metabolites (**Figure 12E)**, further supporting the conclusion that there is lower utilization of glucose-derived carbons in the TCA cycle by Slc7a11$^{sut/sut}$ MuSCs.

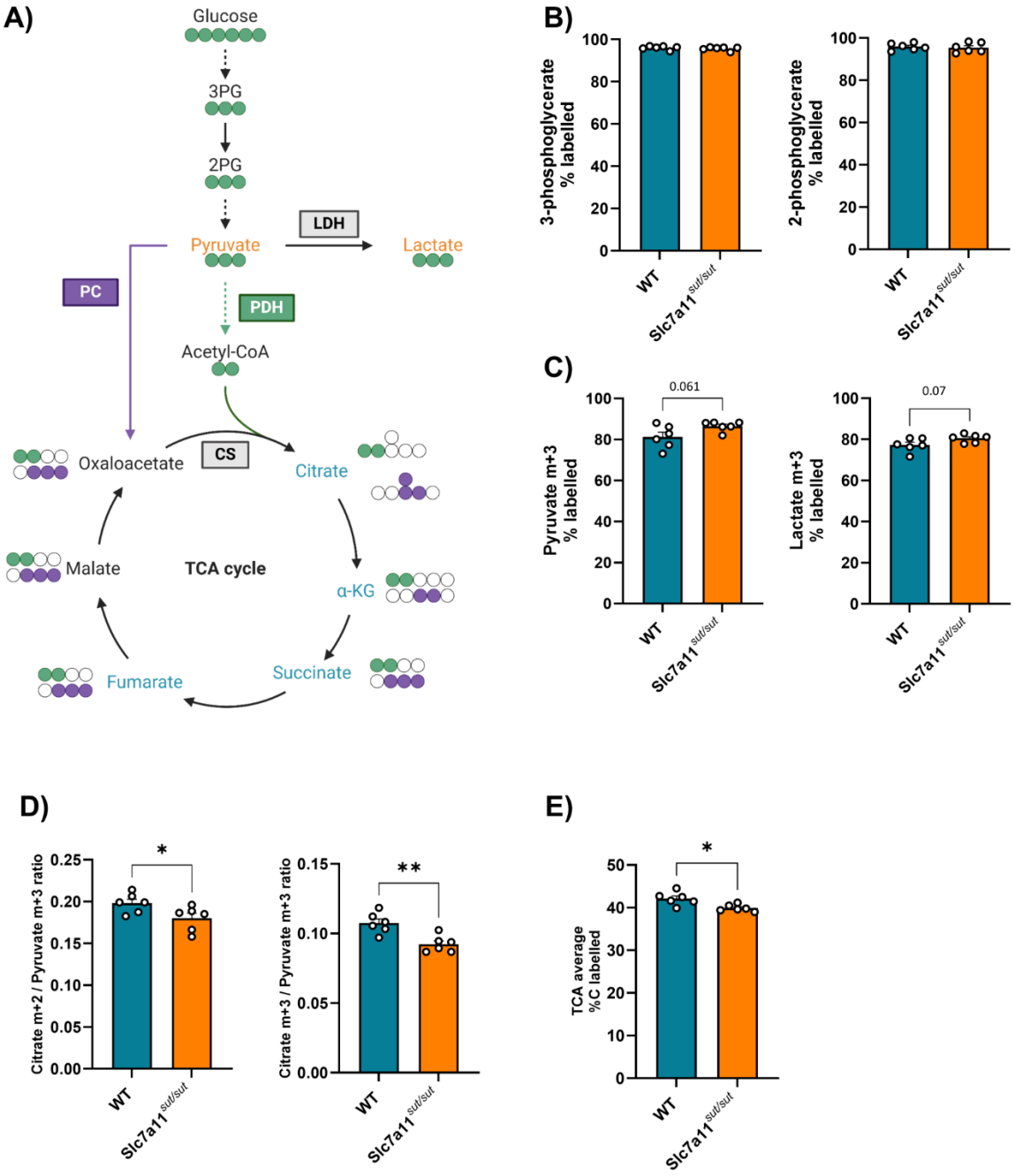
A)
Glucose
3PG
2PG
Pyruvate
LDH
Lactate
PC
PDH
Acetyl-CoA
Oxaloacetate
CS
Citrate
Malate
TCA cycle
α-KG
Fumarate
Succinate
B)
3-phosphoglycerate % labelled
2-phosphoglycerate % labelled
WT
Slc7a11sut/sut
C)
Pyruvate m+3 % labelled
Lactate m+3 % labelled
0.061
0.07
D)
Citrate m+2 / Pyruvate m+3 ratio
Citrate m+3 / Pyruvate m+3 ratio
E)
TCA average %C labelled

Figure 12. Lower glucose flux to TCA cycle in Slc7a11$^{sut/sut}$ MuSCs.
(A) Stable isotope tracing diagram for [U-^{13}C]-Glucose through glycolysis and TCA cycle via pyruvate dehydrogenase (PDH, green) and pyruvate carboxylase (PC, purple). Labelled metabolites are coloured orange (higher in Slc7a11$^{sut/sut}$ MuSCs), blue (lower in Slc7a11$^{sut/sut}$ MuSCs), and black (similar between Slc7a11$^{sut/sut}$ and WT MuSCs). **(B-C)** [U-^{13}C]-Glucose labelling (12 hrs) to glycolytic intermediate metabolites **(B)** 3-phosphoglycerate, and 2-phosphoglycerate, and **(C)** pyruvate m+3 and lactate m+3 in WT and Slc7a11$^{sut/sut}$ MuSCs. **(D)** Citrate m+2 / pyruvate m+3 and citrate m+3 / pyruvate m+3 ratios of [U-^{13}C]-glucose labelling (12 hrs) as proxies of PDH and PC, respectively. **(E)** Relative proportion of labelled TCA cycle intermediates (citrate, α-ketoglutarate, succinate, fumarate, and malate) derived from [U-^{13}C]-glucose precursor. The statistical significance of the differences between groups was determined using a two-tailed Student's t-test, n = 6. Results are presented as mean ± SEM, *p < 0.05, **p < 0.01.

3.2.3 Increased *de novo* serine and cysteine synthesis in Slc7a11$^{sut/sut}$ MuSCs

Glucose also serves as a precursor for *de novo* serine synthesis by converting glycolysis-derived 3PG to 3-phosphohydroxypyruvate in a reaction catalyzed by phosphoglycerate dehydrogenase (PHGDH) [80]. *De novo* serine synthesis is upregulated during times of amino acid starvation, as serine is a major donor to the carbon pool for one-carbon (1C) metabolism, linking the folate and methionine cycles with the transsulfuration pathway to support amino acid metabolism, redox homeostasis, nucleotide biosynthesis, and methylation reactions [81]. Serine 1C metabolism also plays a key role in GSH biosynthesis via endogenous cysteine and glycine biosynthesis [82] (**Figure 13A**). Thus, it was hypothesized that Slc7a11$^{sut/sut}$ MuSCs would have an increased reliance on glycolytic metabolism to support *de novo* synthesis of serine as a compensatory mechanism to restore GSH redox. Consistent with that hypothesis, Slc7a11$^{sut/sut}$ MuSCs had higher serine m+3 levels (from glycolysis-derived 3PG, [83]) compared to WT, indicating an increased serine biosynthesis from glycolysis (**Figure 13B).** Moreover, protein levels of key enzymes involved in *de novo* serine synthesis (PSAT1 and PSPH) were higher in Slc7a11$^{sut/sut}$ MuSCs compared to WT MuSCs (**Figure 13C**). Notably, WT and Slc7a11$^{sut/sut}$ MuSCs had similar m+2 labelling to glycine, suggesting that glucose-derived serine is preferentially shunted towards the transsulfuration pathway for cysteine biosynthesis **(Figure 13D**). Indeed, while expression of cystathionine β-synthase (CBS), which catalyzes the conversion of serine and homocysteine to cystathionine, was comparable between genotypes, the protein level of cystathionine γ-lyase (CTH), which converts cystathionine to cysteine, was higher in Slc7a11$^{sut/sut}$ MuSCs (**Figure 13E**). The levels of GSH m+2 (derived from glycine m+2 or glutamate m+2 incorporation), and GSH m+4 (derived from the incorporation of both glycine m+2 and glutamate m+2) were lower in Slc7a11$^{sut/sut}$

MuSCs (**Figure 13F**). Conversely, the level of GSH m+3 (derived from cysteine m+3 incorporation) was not different between genotypes, suggesting that transsulfuration pathway activity in Slc7a11$^{sut/sut}$ MuSCs resulted in GSH biosynthesis (**Figure 13F**).

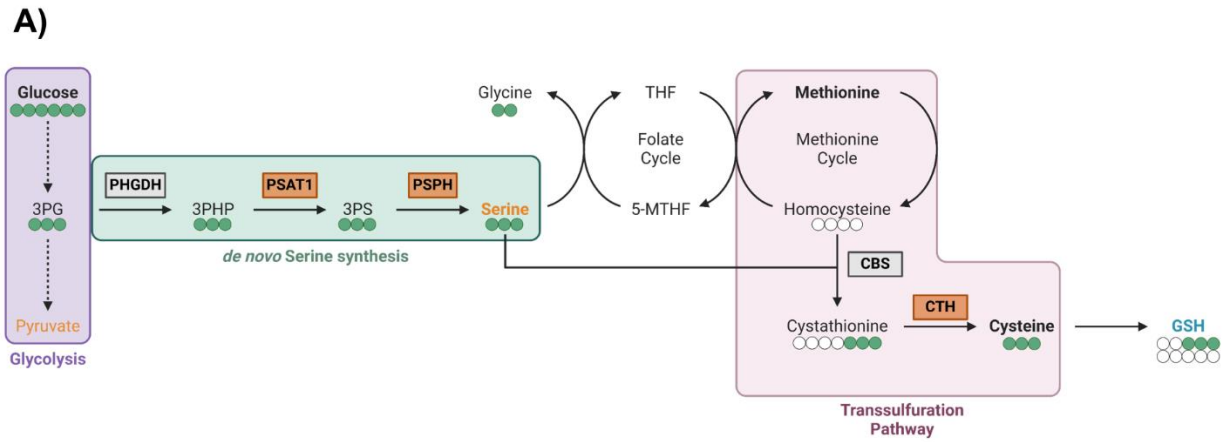
A)
Glucose
3PG
Pyruvate
Glycolysis
PHGDH
3PHP
PSAT1
3PS
PSPH
Serine
de novo Serine synthesis
Glycine
THF
Folate Cycle
5-MTHF
Methionine
Methionine Cycle
Homocysteine
CBS
Cystathionine
CTH
Cysteine
GSH
Transsulfuration Pathway

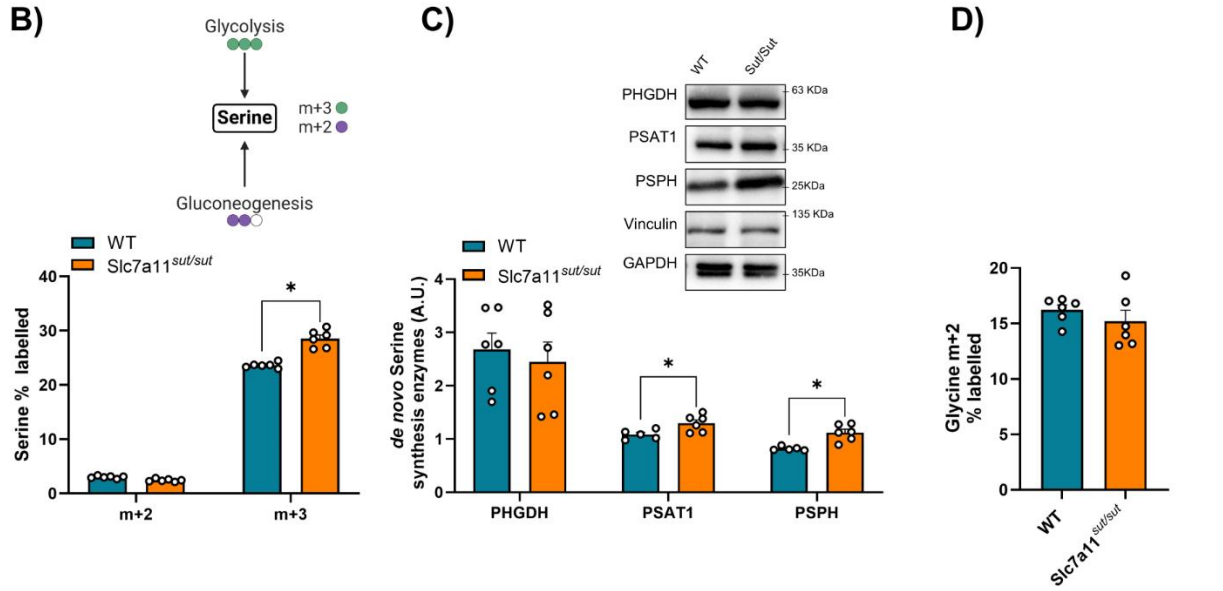
B)
Glycolysis
Serine
m+3
m+2
Gluconeogenesis
WT
Slc7a11sut/sut
Serine % labelled
m+2
m+3
C)
WT
Sut/Sut
PHGDH
63 KDa
PSAT1
35 KDa
PSPH
25KDa
Vinculin
135 KDa
GAPDH
35KDa
WT
Slc7a11sut/sut
de novo Serine synthesis enzymes (A.U.)
PHGDH
PSAT1
PSPH
D)
Glycine m+2 % labelled
WT
Slc7a11sut/sut

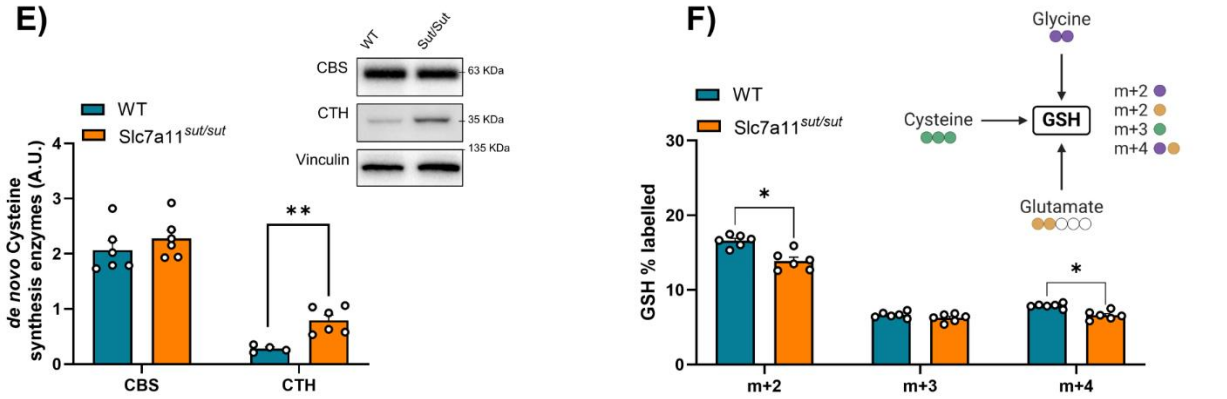
E)
WT
Sut/Sut
CBS
63 KDa
CTH
35 KDa
Vinculin
135 KDa
WT
Slc7a11sut/sut
de novo Cysteine synthesis enzymes (A.U.)
CBS
CTH
F)
Glycine
WT
Slc7a11sut/sut
Cysteine
GSH
m+2
m+2
m+3
m+4
Glutamate
GSH % labelled
m+2
m+3
m+4

Figure 13. xCT deficiency promotes *de novo* serine synthesis.
(A) [U-^{13}C]-glucose labelling through the *de novo* serine synthesis pathway, and cysteine biosynthesis via the transsulfuration pathway. Enzymes and labelled metabolites are coloured orange (higher in Slc7a11$^{sut/sut}$ MuSCs), blue (lower in Slc7a11$^{sut/sut}$ MuSCs), and black (similar between Slc7a11$^{sut/sut}$ and WT MuSCs). **(B)** [U-^{13}C]-glucose labelling (12 hrs) of serine m+2 (from gluconeogenesis) and serine m+3 (from glycolysis) expressed as percentage of total respective metabolite levels. **(C)** Immunoblot of *de novo* serine synthesis enzymes (PHGDH, PSAT1, and PSPH). **(D)** [U-^{13}C]-glucose labelling (12 hrs) of glycine m+2, expressed as labelled percentage of total glycine levels. **(E)** Immunoblot of *de novo* cysteine synthesis enzymes (CBS and CTH). **(F)** [U-^{13}C]-glucose labelling (12 hrs) of GSH m+2 (from [U-^{13}C]-glucose-derived glycine or glutamate), GSH m+3 (from [U-^{13}C]-glucose-derived cysteine), and GSH m+4 (from [U-^{13}C]-glucose derived glycine and glutamate). The statistical significance of the differences between groups was determined using a two-tailed Student's t-test, n = 6. Results are presented as mean ± SEM, *$p < 0.05$, **$p < 0.01$, ***$p < 0.001$, ****$p < 0.0001$.

3.3 Disrupted cystine import enhances SKM differentiation

To investigate the impact of disrupted cystine import on myogenesis, immunostaining analyses were performed in cultured MuSCs and *ex vivo* myofibers. Immunostaining for cell proliferation markers showed lower proportions of $Pax7^{+}$ Edu^{+} cells in proliferating $Slc7a11^{sut/sut}$ MuSCs compared to WT (**Figure 14A**). Staining for myosin (MYH) revealed elevated MYH^{+} area in $Slc7a11^{sut/sut}$ MuSCs compared to WT at early differentiation, indicating a more rapid differentiation in $Slc7a11^{sut/sut}$ MuSCs (**Figure 14B**). Finally, hematoxylin and eosin staining in SKM myofibers, 21 days after cardiotoxin damage, demonstrated increased myofiber cross-sectional area (CSA) in $Slc7a11^{sut/sut}$ MuSCs compared to WT (**Figure 14C**). Collectively, these data are consistent with the conclusion that disruption in cystine import is related to increased myogenesis.

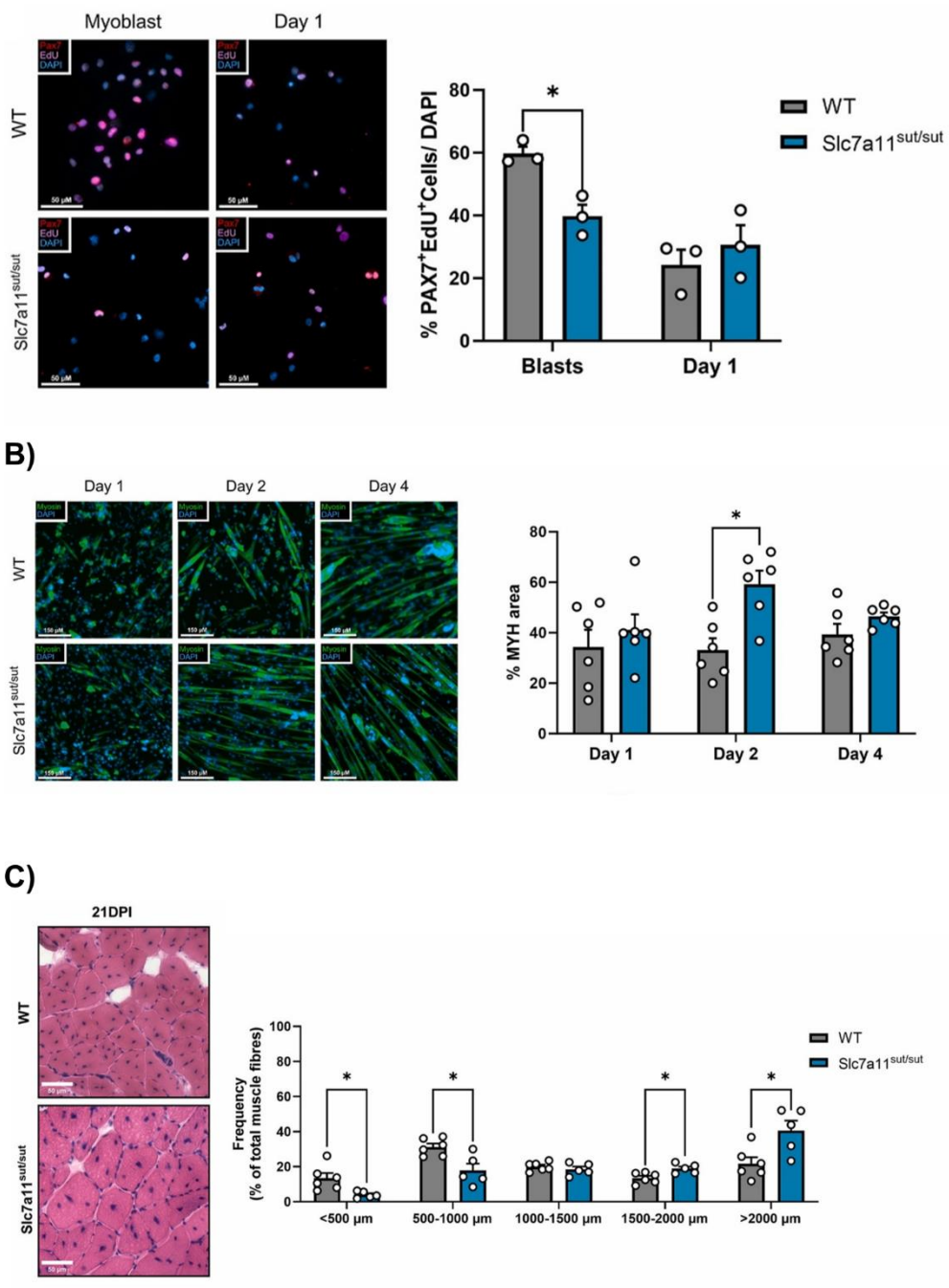
A)
Myoblast
Day 1
WT
Slc7a11sut/sut
Pax7
EdU
DAPI
% PAX7+EdU+Cells/ DAPI
Blasts
Day 1
WT
Slc7a11sut/sut
B)
Day 1
Day 2
Day 4
Myosin
DAPI
% MYH area
C)
21DPI
Frequency (% of total muscle fibres)
<500 µm
500-1000 µm
1000-1500 µm
1500-2000 µm
>2000 µm
Average CSA (µm2)

Figure 14. xCT dysfunction promotes higher MuSC differentiation rate.
(A) Immunofluorescence analyses of Pax7 (red), EdU+ (purple), and DAPI (blue) in proliferating myoblasts and myotubes at day 1 of differentiation, scale bar = 50 μm, n = 3. **(B)** Immunofluorescence analyses of myosin (green) and DAPI (blue) in differentiating myotubes at days 1, 2, and 4 of differentiation. The myosin-positive area as a percent of the total area analyzed is plotted, scale bar = 150 μm, n = 6. **(C)** Hematoxylin and eosin (H&E) staining of muscle sections from TA muscles after 21 days of cardiotoxin injection (21DPI). Frequency distribution of myofiber cross-sectional area (CSA) and average myofiber CSA are plotted. Scale bar = 50 μm, n = 5–6. The statistical significance of the differences between groups was determined using a two-tailed Student's t-test. Results are presented as mean ± SEM, *$p < 0.05$.

CHAPTER 4: DISCUSSION

This work provides an important link between cyst(e)ine and muscle health. Disrupted cystine import via xCT in MuSCs led to perturbations in GSH redox and mitochondrial structure/function, accompanied by broad metabolic reprogramming marked by increased TSP activity (**Figure 15**).

Mitochondria are major sites of cellular ROS production with complexes I and III of the ETC being the major sites of superoxide release. Superoxide is rapidly converted to H_2O_2, which has a longer half-life and can traverse membranes [84]. The proportion of ROS generated from mitochondrial respiration varies based on the activity of the OXPHOS system [85]. Here, findings show higher H_2O_2 emissions and lower GSH levels as a result of disrupted cystine import, consistent with perturbed MuSC redox homeostasis. Concomitantly, cells had lower OXPHOS activity and derived a greater proportion of ATP from glycolysis. These findings are consistent with the possibility that $Slc7a11^{sut/sut}$ MuSCs downregulate mitochondrial activity in an effort to restore redox balance. Consistent with this possibility, SITA of [U-^{13}C]-glucose showed accumulation of pyruvate and lower TCA cycle entry through both PC and PDH. These findings are in accordance with previous reports in cancer cells, where ROS stabilized hypoxia inducible factor 1α (HIF-1α) even under normal O_2 concentrations, thereby inducing the phosphorylation and inhibition of PDH by PDH kinase 1 (PDK1), ultimately leading to lower pyruvate entry to the TCA cycle [86–88]. This preference for glycolysis observed in cancer cells was first described by Otto Warburg [89]. While glycolysis is an inefficient way of producing ATP, it does generate necessary glycolytic intermediates for the biosynthesis of other molecules via the pentose phosphate pathway (PPP), and in the case of $Slc7a11^{sut/sut}$ MuSCs, *de novo* serine and cysteine via the TSP [21].

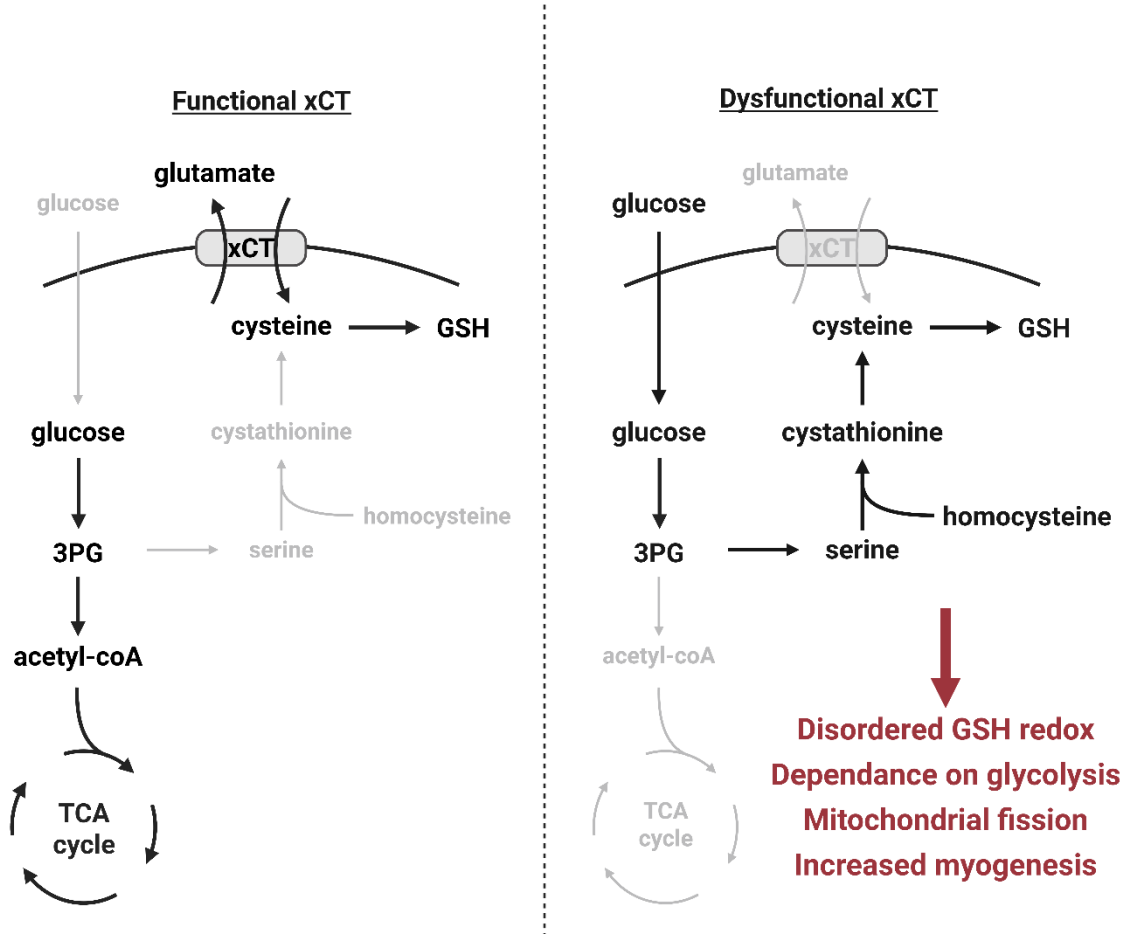

Figure 15. Metabolic consequences of disrupted cystine import via xCT.

Many studies have examined the link between mitochondrial dynamics and cellular dysfunction in diseases. Indeed, downregulation of OPA1 results in mitochondrial dysfunction in mouse embryonic fibroblasts (MEFs) [90] and increased susceptibility to apoptosis in HeLa cells [91]. Patients with heterozygous mutations in *Mfn2* have Charcot-Marie-Tooth type 2A, a disease characterized by muscle atrophy and weakness [92]. Mouse SKM with conditional deletion of Mfn1 and Mfn2 was shown to have impaired respiratory functions [93]. Here, increased Drp1-mediated fission and lower OXPHOS rates were observed in Slc7a11$^{sut/sut}$ MuSCs, which is in accordance with previous reports showing how mild oxidative stress leads to mitochondrial fission [94]. Slc7a11$^{sut/sut}$ MuSCs demonstrated elevated H_2O_2 emissions across multiple mitochondrial metabolic states. Similarly, previous reports in C2C12 SKM myoblasts showed that exposure to exogenous H_2O_2 led to mitochondrial fission preceded by changes in inner mitochondrial membrane potential, and suggested that mitochondrial depolarization could promote fission [54]. In fact, a growing body of evidence supports the role of ROS in promoting mitochondrial fission [95–99]. During times of oxidative stress, protein kinase Cδ (PKCδ) stimulates DRP1 Ser616 phosphorylation, leading to mitochondrial fission [100]. Mechanistically, GSH seems to play an important yet ambiguous role in mitochondrial dynamics. For example, in primary human fibroblasts, the inhibition of GSH synthesis with buthionine sulfoximine (BSO) prompted a decrease in mitochondrial size accompanied by increased oxidation of molecular probes such as roGFP1 and CM-H_2DCF [101]. In contrast, BSO treatment in HeLa cancer cells prompted GSSG-induced Mfn oligomerization, leading to mitochondrial hyperfusion [102]. Interestingly, consistent with the increased Drp1 oligomerization in Slc7a11$^{sut/sut}$ MuSCs, another study in endothelial cells reported that high ROS induced Drp1 oligomerization and subsequently, mitochondrial

fragmentation [103]. This further suggests that GSH-linked mitochondrial morphological changes may be cell type and context-dependent.

Additionally, the author of this thesis hypothesizes that mitochondrial fission could play a beneficial role in preventing a vicious feed forward loop of ROS-induced ROS release by mitochondrial NADPH oxidases. Other than the ETC, NADPH oxidases are important sources of ROS production [104,105], as they catalyze the 1-electron reduction of O_2 using NADH or NADPH [106]. Under certain conditions, mitochondrial ROS generated by the ETC can stimulate NADPH oxidases; however, the exact mechanism remains unclear [107–110]. Since some reports describe that mitochondrial fragmentation leads to disrupted respiration [93], fission could serve as a way to halt further generation of ROS from the ETC and NADPH oxidases via a positive-feedback loop.

Fusion/fission have been shown to be crucial for adaptation to cellular stress. Interestingly, fusion was shown to protect mitochondria from autophagy during nutrient—especially amino acid—starvation [111,112]. This goes contrary to the observations here of increased fission in MuSCs with disrupted cystine uptake, which speaks to the complexity of mitochondrial dynamics regulation within the cell. Ultimately, it seems ROS-related signaling prevailed in this “tug-of-war”, leading to increased Drp1-mediated fission. Finally, although this work (and many others in the literature) describes decreased OXPHOS with mitochondrial fission, it is important to note that it is not yet clearly established whether fused or fragmented mitochondria perform “better” bioenergetically [74]. Therefore, this complex interplay also relies on other important cellular cues.

Slc7a11$^{sut/sut}$ MuSCs also demonstrated a remarkable increase in glucose uptake, despite a trend for lower glycolytic flux and lower OXPHOS and CS activities. Other researchers have shown that contracting SKM has increased ROS-mediated glucose uptake [113,114]. Higher glucose uptake could provide Slc7a11$^{sut/sut}$ cells with multiple advantages in response to impaired cystine uptake. Although overall GSH levels were still lower in Slc7a11$^{sut/sut}$ compared to WT, increased GSH m+3 levels (coming from [U-^{13}C]-glucose labeled cysteine) demonstrate that the TSP was partially effective at restoring GSH homeostasis. Therefore, with limited pyruvate entry to the TCA cycle, and a "pull" of glycolytic carbons into the TSP due to increased GSH demand, higher glucose uptake might further drive *de novo* serine synthesis by "flooding" the TSP pathway according to Le Chatelier's principle.

A potentially desirable outcome of TSP activity is the generation of hydrogen sulfide (H_2S), which is a gaseous signaling molecule that exerts anti-inflammatory and antioxidant functions [115]. In mice, NaHS treatment, a H_2S donor, proved effective at alleviating some symptoms of Duchenne muscular dystrophy, which is an incurable (at the time of writing this thesis), deadly disease caused by a mutation to the gene that encodes dystrophin [116]. Endogenous H_2S is mainly produced by CBS and CTH, both enzymes of the TSP, either as a by-product of their activities, or in separate reactions catalyzed by these enzymes [117]. Here, Slc7a11$^{sut/sut}$ MuSCs displayed elevated CTH protein levels, which is likely leading to higher endogenous H_2S production. While no H_2S measurements were performed in this work, the author hypothesizes that it could be driving higher differentiation/regeneration rates observed in myotubes. Indeed, Slc7a11$^{sut/sut}$ MuSCs cultured *in vitro* had lower proliferation and higher differentiation rates as evidenced by immunostaining, and higher TSP rates as evidenced by [U-^{13}C]-glucose SITA. Similar effects of H_2S enhancing myogenic differentiation were

recently described in C2C12 myoblasts [118]. However, it is important to note that cells often behave differently *in vivo* than *in vitro*; that C2C12 cells are a transformed mouse muscle cell line and that TSP-independent systemic adaptive mechanisms could be utilized to compensate for disrupted cystine uptake in tissues and lead to the observed enhanced myogenesis in Slc7a11$^{sut/sut}$ SKM. The importance of TSP enzymes and H_2S *in vivo* is not yet fully known. This is partially due to the discrepancies in different models; for example, human SKM expresses similar levels of CBS and CTH relative to liver expression, while mice SKM completely lack these enzymes compared to liver expression [119]. Strikingly, Slc7a11$^{sut/sut}$ MuSCs clearly demonstrated increased use of TSP enzymes, as evidenced by [U-^{13}C]-glucose SITA and increased CTH protein levels. Whether this discrepancy is due to *in vitro* adaptations of MuSCs, poor quality analyses of published studies [119–121], or mouse strain differences [115], is unknown. Ultimately, myogenesis is a complex process and further research is needed to understand the involvement of the TSP in the context of redox imbalances.

CHAPTER 5: CONCLUSION

In conclusion, findings highlight the dual role of xCT in regulating redox balance and metabolic reprogramming in proliferating MuSCs. Slc7a11$^{sut/sut}$ MuSCs had a profound metabolic reprogramming characterized by lower TCA cycle activity and increased glucose uptake and flux towards *de novo* serine synthesis. These metabolic changes, driven by lower GSH levels were accompanied by increased mitochondrial fragmentation and evidence for faster myogenesis. While GSH levels were partially restored through *de novo* cysteine synthesis from glucose, the observed metabolic changes underscore the crucial role of xCT in muscle metabolism and GSH redox. Muscular dystrophies are complex diseases; however, novel therapeutic approaches may be derived from the targeting of metabolic pathways in SKM. For example, a recent study showed how a combined pharmacological-exercise treatment can potentiate rescue in mice with type I myotonic dystrophy by reversing alternative splicing events and promoting oxidative metabolism in SKM [122]. Beyond its established function in redox homeostasis, xCT holds a critical metabolic function in muscle cells, providing insights that may inform future therapeutic strategies for muscular pathologies.

BIBLIOGRAPHY

[1] W.R. Frontera, J. Ochala, Skeletal Muscle: A Brief Review of Structure and Function, Calcif. Tissue Int. 96 (2015) 183–195. https://doi.org/10.1007/s00223-014-9915-y.

[2] C.A.C. Ottenheijm, H. Granzier, Lifting the Nebula: Novel Insights into Skeletal Muscle Contractility, Physiology 25 (2010) 304–310. https://doi.org/10.1152/physiol.00016.2010.

[3] J.A. Monroy, K.L. Powers, L.A. Gilmore, T.A. Uyeno, S.L. Lindstedt, K.C. Nishikawa, What Is the Role of Titin in Active Muscle?, Exerc. Sport Sci. Rev. 40 (2012) 73. https://doi.org/10.1097/JES.0b013e31824580c6.

[4] G.D. Thomas, Functional muscle ischemia in Duchenne and Becker muscular dystrophy, Front. Physiol. 4 (2013). https://doi.org/10.3389/fphys.2013.00381.

[5] K.E. Merz, D.C. Thurmond, Role of Skeletal Muscle in Insulin Resistance and Glucose Uptake, in: Compr. Physiol., John Wiley & Sons, Ltd, 2020: pp. 785–809. https://doi.org/10.1002/cphy.c190029.

[6] J. Talbot, L. Maves, Skeletal muscle fiber type: using insights from muscle developmental biology to dissect targets for susceptibility and resistance to muscle disease, WIREs Dev. Biol. 5 (2016) 518–534. https://doi.org/10.1002/wdev.230.

[7] G. Gouspillou, N. Sgarioto, B. Norris, S. Barbat-Artigas, M. Aubertin-Leheudre, J.A. Morais, Y. Burelle, T. Taivassalo, R.T. Hepple, The Relationship between Muscle Fiber Type-Specific PGC-1α Content and Mitochondrial Content Varies between Rodent Models and Humans, PLOS ONE 9 (2014) e103044. https://doi.org/10.1371/journal.pone.0103044.

[8] N. Ørtenblad, J. Nielsen, R. Boushel, K. Söderlund, B. Saltin, H.-C. Holmberg, The Muscle Fiber Profiles, Mitochondrial Content, and Enzyme Activities of the Exceptionally Well-Trained Arm and Leg Muscles of Elite Cross-Country Skiers, Front. Physiol. 9 (2018). https://doi.org/10.3389/fphys.2018.01031.

[9] J. Nunnari, A. Suomalainen, Mitochondria: In Sickness and in Health, Cell 148 (2012) 1145–1159. https://doi.org/10.1016/j.cell.2012.02.035.

[10] C. Jose, S. Melser, G. Benard, R. Rossignol, Mitoplasticity: Adaptation Biology of the Mitochondrion to the Cellular Redox State in Physiology and Carcinogenesis, Antioxid. Redox Signal. 18 (2013) 808–849. https://doi.org/10.1089/ars.2011.4357.

[11] C. Hönscher, M. Mari, K. Auffarth, M. Bohnert, J. Griffith, W. Geerts, M. van der Laan, M. Cabrera, F. Reggiori, C. Ungermann, Cellular Metabolism Regulates Contact Sites between Vacuoles and Mitochondria, Dev. Cell 30 (2014) 86–94. https://doi.org/10.1016/j.devcel.2014.06.006.

[12] M.A. Frohman, Mitochondria as integrators of signal transduction and energy production in cardiac physiology and disease, J. Mol. Med. 88 (2010) 967–970. https://doi.org/10.1007/s00109-010-0662-x.

[13] M.B. Bell, Z. Bush, G.R. McGinnis, G.C. Rowe, Adult skeletal muscle deletion of Mitofusin 1 and 2 impedes exercise performance and training capacity, J. Appl. Physiol. 126 (2019) 341–353. https://doi.org/10.1152/japplphysiol.00719.2018.

[14] D.-F. Suen, K.L. Norris, R.J. Youle, Mitochondrial dynamics and apoptosis, Genes Dev. 22 (2008) 1577–1590. https://doi.org/10.1101/gad.1658508.

[15] D.C. Chan, Fusion and Fission: Interlinked Processes Critical for Mitochondrial Health, Annu. Rev. Genet. 46 (2012) 265–287. https://doi.org/10.1146/annurev-genet-110410-132529.
[16] S. Tajbakhsh, Skeletal muscle stem cells in developmental versus regenerative myogenesis, J. Intern. Med. 266 (2009) 372–389. https://doi.org/10.1111/j.1365-2796.2009.02158.x.
[17] S.B.P. Chargé, M.A. Rudnicki, Cellular and Molecular Regulation of Muscle Regeneration, Physiol. Rev. 84 (2004) 209–238. https://doi.org/10.1152/physrev.00019.2003.
[18] H. Yin, F. Price, M.A. Rudnicki, Satellite Cells and the Muscle Stem Cell Niche, Physiol. Rev. 93 (2013) 23–67. https://doi.org/10.1152/physrev.00043.2011.
[19] E. Le Moal, V. Pialoux, G. Juban, C. Groussard, H. Zouhal, B. Chazaud, R. Mounier, Redox Control of Skeletal Muscle Regeneration, Antioxid. Redox Signal. 27 (2017) 276–310. https://doi.org/10.1089/ars.2016.6782.
[20] A.H. Tang, T.A. Rando, Induction of autophagy supports the bioenergetic demands of quiescent muscle stem cell activation, EMBO J. 33 (2014) 2782–2797. https://doi.org/10.15252/embj.201488278.
[21] J.G. Ryall, Metabolic reprogramming as a novel regulator of skeletal muscle development and regeneration, FEBS J. 280 (2013) 4004–4013. https://doi.org/10.1111/febs.12189.
[22] J. Smeitink, L. van den Heuvel, S. DiMauro, The genetics and pathology of oxidative phosphorylation, Nat. Rev. Genet. 2 (2001) 342–352. https://doi.org/10.1038/35072063.
[23] N. Collao, P. Akohene-Mensah, J. Nallabelli, E.R. Binet, A. Askarian, J. Lloyd, G.M. Niemiro, J.W. Beals, S. van Vliet, R. Rajgara, A. Saleh, N. Wiper-Bergeron, S.A. Paluska, N.A. Burd, M. De Lisio, The role of L-type amino acid transporter 1 (Slc7a5) during in vitro myogenesis, Am. J. Physiol. Cell Physiol. 323 (2022) C595–C605. https://doi.org/10.1152/ajpcell.00162.2021.
[24] M.P. Murphy, A. Holmgren, N.-G. Larsson, B. Halliwell, C.J. Chang, B. Kalyanaraman, S.G. Rhee, P.J. Thornalley, L. Partridge, D. Gems, T. Nyström, V. Belousov, P.T. Schumacker, C.C. Winterbourn, Unraveling the Biological Roles of Reactive Oxygen Species, Cell Metab. 13 (2011) 361–366. https://doi.org/10.1016/j.cmet.2011.03.010.
[25] C.L. Bigarella, R. Liang, S. Ghaffari, Stem cells and the impact of ROS signaling, Development 141 (2014) 4206–4218. https://doi.org/10.1242/dev.107086.
[26] C. Henríquez-Olguín, S. Gallero, A. Reddy, K.W. Persson, F.L. Schlabs, C.T. Voldstedlund, G. Valentinaviciute, R. Meneses-Valdés, C.M. Sigvardsen, B. Kiens, E.T. Chouchani, E.A. Richter, T.E. Jensen, Revisiting insulin-stimulated hydrogen peroxide dynamics reveals a cytosolic reductive shift in skeletal muscle, Redox Biol. 82 (2025) 103607. https://doi.org/10.1016/j.redox.2025.103607.
[27] D.P. Jones, Redefining Oxidative Stress, Antioxid. Redox Signal. 8 (2006) 1865–1879. https://doi.org/10.1089/ars.2006.8.1865.
[28] E.B. Tahara, F.D.T. Navarete, A.J. Kowaltowski, Tissue-, substrate-, and site-specific characteristics of mitochondrial reactive oxygen species generation, Free Radic. Biol. Med. 46 (2009) 1283–1297. https://doi.org/10.1016/j.freeradbiomed.2009.02.008.
[29] M. Schieber, N.S. Chandel, ROS Function in Redox Signaling and Oxidative Stress, Curr. Biol. 24 (2014) R453–R462. https://doi.org/10.1016/j.cub.2014.03.034.

[30] F.L. Grand, A.E. Jones, V. Seale, A. Scimè, M.A. Rudnicki, Wnt7a Activates the Planar Cell Polarity Pathway to Drive the Symmetric Expansion of Satellite Stem Cells, Cell Stem Cell 4 (2009) 535–547. https://doi.org/10.1016/j.stem.2009.03.013.
[31] G. Zaccagnini, F. Martelli, A. Magenta, C. Cencioni, P. Fasanaro, C. Nicoletti, P. Biglioli, P.G. Pelicci, M.C. Capogrossi, p66ShcA and Oxidative Stress Modulate Myogenic Differentiation and Skeletal Muscle Regeneration after Hind Limb Ischemia *, J. Biol. Chem. 282 (2007) 31453–31459. https://doi.org/10.1074/jbc.M702511200.
[32] N.S. Rajasekaran, S.B. Shelar, D.P. Jones, J.R. Hoidal, Reductive stress impairs myogenic differentiation, Redox Biol. 34 (2020) 101492. https://doi.org/10.1016/j.redox.2020.101492.
[33] B. Halliwell, J.M.C. Gutteridge, Free Radicals in Biology and Medicine, Oxford University Press, 2015.
[34] H.J. Forman, H. Zhang, A. Rinna, Glutathione: Overview of its protective roles, measurement, and biosynthesis, Mol. Aspects Med. 30 (2009) 1–12. https://doi.org/10.1016/j.mam.2008.08.006.
[35] S.C. Lu, Glutathione synthesis, Biochim. Biophys. Acta BBA - Gen. Subj. 1830 (2013) 3143–3153. https://doi.org/10.1016/j.bbagen.2012.09.008.
[36] F.Q. Schafer, G.R. Buettner, Redox environment of the cell as viewed through the redox state of the glutathione disulfide/glutathione couple, Free Radic. Biol. Med. 30 (2001) 1191–1212. https://doi.org/10.1016/S0891-5849(01)00480-4.
[37] I. Dalle-Donne, R. Rossi, G. Colombo, D. Giustarini, A. Milzani, Protein *S*-glutathionylation: a regulatory device from bacteria to humans, Trends Biochem. Sci. 34 (2009) 85–96. https://doi.org/10.1016/j.tibs.2008.11.002.
[38] B.D. Paul, J.I. Sbodio, S.H. Snyder, Cysteine Metabolism in Neuronal Redox Homeostasis, Trends Pharmacol. Sci. 39 (2018) 513–524. https://doi.org/10.1016/j.tips.2018.02.007.
[39] A. Miseta, P. Csutora, Relationship Between the Occurrence of Cysteine in Proteins and the Complexity of Organisms, Mol. Biol. Evol. 17 (2000) 1232–1239. https://doi.org/10.1093/oxfordjournals.molbev.a026406.
[40] M.S. Vandiver, B.D. Paul, R. Xu, S. Karuppagounder, F. Rao, A.M. Snowman, H. Seok Ko, Y. Il Lee, V.L. Dawson, T.M. Dawson, N. Sen, S.H. Snyder, Sulfhydration mediates neuroprotective actions of parkin, Nat. Commun. 4 (2013) 1626. https://doi.org/10.1038/ncomms2623.
[41] N. Sen, B.D. Paul, M.M. Gadalla, A.K. Mustafa, T. Sen, R. Xu, S. Kim, S.H. Snyder, Hydrogen Sulfide-Linked Sulfhydration of NF-κB Mediates Its Antiapoptotic Actions, Mol. Cell 45 (2012) 13–24. https://doi.org/10.1016/j.molcel.2011.10.021.
[42] A.K. Mustafa, M.M. Gadalla, N. Sen, S. Kim, W. Mu, S.K. Gazi, R.K. Barrow, G. Yang, R. Wang, S.H. Snyder, H2S Signals Through Protein S-Sulfhydration, Sci. Signal. 2 (2009) ra72–ra72. https://doi.org/10.1126/scisignal.2000464.
[43] J. Zhu, M. Berisa, S. Schwörer, W. Qin, J.R. Cross, C.B. Thompson, Transsulfuration Activity Can Support Cell Growth upon Extracellular Cysteine Limitation, Cell Metab. 30 (2019) 865-876.e5. https://doi.org/10.1016/j.cmet.2019.09.009.
[44] J. Lewerenz, S.J. Hewett, Y. Huang, M. Lambros, P.W. Gout, P.W. Kalivas, A. Massie, I. Smolders, A. Methner, M. Pergande, S.B. Smith, V. Ganapathy, P. Maher, The Cystine/Glutamate Antiporter System xc− in Health and Disease: From Molecular

Mechanisms to Novel Therapeutic Opportunities, Antioxid. Redox Signal. 18 (2013) 522–555. https://doi.org/10.1089/ars.2011.4391.
[45] M.D. Pizzagalli, A. Bensimon, G. Superti-Furga, A guide to plasma membrane solute carrier proteins, FEBS J. 288 (2021) 2784–2835. https://doi.org/10.1111/febs.15531.
[46] P.K. Mandal, A. Seiler, T. Perisic, P. Kölle, A. Banjac Canak, H. Förster, N. Weiss, E. Kremmer, M.W. Lieberman, S. Bannai, P. Kuhlencordt, H. Sato, G.W. Bornkamm, M. Conrad, System xc− and Thioredoxin Reductase 1 Cooperatively Rescue Glutathione Deficiency*, J. Biol. Chem. 285 (2010) 22244–22253. https://doi.org/10.1074/jbc.M110.121327.
[47] Y. Huang, Z. Dai, C. Barbacioru, W. Sadée, Cystine-Glutamate Transporter SLC7A11 in Cancer Chemosensitivity and Chemoresistance, Cancer Res. 65 (2005) 7446–7454. https://doi.org/10.1158/0008-5472.CAN-04-4267.
[48] M. Lo, Y.-Z. Wang, P.W. Gout, The x cystine/glutamate antiporter: A potential target for therapy of cancer and other diseases, J. Cell. Physiol. 215 (2008) 593–602. https://doi.org/10.1002/jcp.21366.
[49] R.-S. Chen, Y.-M. Song, Z.-Y. Zhou, T. Tong, Y. Li, M. Fu, X.-L. Guo, L.-J. Dong, X. He, H.-X. Qiao, Q.-M. Zhan, W. Li, Disruption of xCT inhibits cancer cell metastasis via the caveolin-1/β-catenin pathway, Oncogene 28 (2009) 599–609. https://doi.org/10.1038/onc.2008.414.
[50] D.D. Bundel, A. Schallier, E. Loyens, R. Fernando, H. Miyashita, J.V. Liefferinge, K. Vermoesen, S. Bannai, H. Sato, Y. Michotte, I. Smolders, A. Massie, Loss of System xc− Does Not Induce Oxidative Stress But Decreases Extracellular Glutamate in Hippocampus and Influences Spatial Working Memory and Limbic Seizure Susceptibility, J. Neurosci. 31 (2011) 5792–5803. https://doi.org/10.1523/JNEUROSCI.5465-10.2011.
[51] A.L. Sheldon, M.B. Robinson, The role of glutamate transporters in neurodegenerative diseases and potential opportunities for intervention, Neurochem. Int. 51 (2007) 333–355. https://doi.org/10.1016/j.neuint.2007.03.012.
[52] N.A. Jackman, T.F. Uliasz, J.A. Hewett, S.J. Hewett, Regulation of System xc−Activity and Expression in Astrocytes by Interleukin-1β, Glia 58 (2010) 1806–1815. https://doi.org/10.1002/glia.21050.
[53] A.E. Allen, Y. Sun, F. Wei, M.A. Reid, J.W. Locasale, Nucleotide metabolism is linked to cysteine availability, J. Biol. Chem. 299 (2023) 103039. https://doi.org/10.1016/j.jbc.2023.103039.
[54] X. Fan, R. Hussien, G.A. Brooks, H2O2-induced mitochondrial fragmentation in C2C12 myocytes, Free Radic. Biol. Med. 49 (2010) 1646–1654. https://doi.org/10.1016/j.freeradbiomed.2010.08.024.
[55] M. Kozakowska, K. Pietraszek-Gremplewicz, A. Jozkowicz, J. Dulak, The role of oxidative stress in skeletal muscle injury and regeneration: focus on antioxidant enzymes, J. Muscle Res. Cell Motil. 36 (2015) 377–393. https://doi.org/10.1007/s10974-015-9438-9.
[56] M.N. Kanaan, C.A. Pileggi, C.Y. Karam, L.S. Kennedy, C. Fong-McMaster, M. Cuperlovic-Culf, M.-E. Harper, Cystine/glutamate antiporter xCT controls skeletal muscle glutathione redox, bioenergetics and differentiation, Redox Biol. 73 (2024) 103213. https://doi.org/10.1016/j.redox.2024.103213.

[57] A. Shahini, K. Vydiam, D. Choudhury, N. Rajabian, T. Nguyen, P. Lei, S.T. Andreadis, Efficient and high yield isolation of myoblasts from skeletal muscle, Stem Cell Res. 30 (2018) 122–129. https://doi.org/10.1016/j.scr.2018.05.017.
[58] A. Liaghati, C.A. Pileggi, G. Parmar, D.A. Patten, N. Hadzimustafic, A. Cuillerier, K.J. Menzies, Y. Burelle, M.-E. Harper, Grx2 Regulates Skeletal Muscle Mitochondrial Structure and Autophagy, Front. Physiol. 12 (2021). https://doi.org/10.3389/fphys.2021.604210.
[59] R. Godin, F. Daussin, S. Matecki, T. Li, B.J. Petrof, Y. Burelle, Peroxisome proliferator-activated receptor γ coactivator 1-α gene transfer restores mitochondrial biomass and improves mitochondrial calcium handling in post-necrotic mdx mouse skeletal muscle, J. Physiol. 590 (2012) 5487–5502. https://doi.org/10.1113/jphysiol.2012.240390.
[60] S.A. Mookerjee, D.G. Nicholls, M.D. Brand, Determining Maximum Glycolytic Capacity Using Extracellular Flux Measurements, PLoS ONE 11 (2016) e0152016. https://doi.org/10.1371/journal.pone.0152016.
[61] M.N. Kanaan, C.A. Pileggi, C.Y. Karam, L.S. Kennedy, C. Fong-McMaster, M. Cuperlovic-Culf, M.-E. Harper, Cystine/glutamate antiporter xCT controls skeletal muscle glutathione redox, bioenergetics and differentiation, Redox Biol. 73 (2024) 103213. https://doi.org/10.1016/j.redox.2024.103213.
[62] A. Chaudhry, R. Shi, D.S. Luciani, A pipeline for multidimensional confocal analysis of mitochondrial morphology, function, and dynamics in pancreatic β-cells, Am. J. Physiol.-Endocrinol. Metab. 318 (2020) E87–E101. https://doi.org/10.1152/ajpendo.00457.2019.
[63] S. McGuirk, Y. Audet-Delage, M.G. Annis, Y. Xue, M. Vernier, K. Zhao, C. St-Louis, L. Minarrieta, D.A. Patten, G. Morin, C.M. Greenwood, V. Giguère, S. Huang, P.M. Siegel, J. St-Pierre, Resistance to different anthracycline chemotherapeutics elicits distinct and actionable primary metabolic dependencies in breast cancer, eLife 10 (2021) e65150. https://doi.org/10.7554/eLife.65150.
[64] C. Menzies, S. Naz, D. Patten, T. Alquier, B.M. Bennett, B. Lacoste, Distinct Basal Metabolism in Three Mouse Models of Neurodevelopmental Disorders, eNeuro 8 (2021). https://doi.org/10.1523/ENEURO.0292-20.2021.
[65] R Core team, R: A Language and Environment for Statistical Computing, R Foundation for Statistical Computing, Vienna, Austria, (2021). https://www.r-project.org/.
[66] J.D. Hunter, Matplotlib: A 2D Graphics Environment, Comput. Sci. Eng. 9 (2007) 90–95. https://doi.org/10.1109/MCSE.2007.55.
[67] H. Wickham, ggplot2, Springer International Publishing, Cham, 2016. https://doi.org/10.1007/978-3-319-24277-4.
[68] P. Virtanen, R. Gommers, T.E. Oliphant, M. Haberland, T. Reddy, D. Cournapeau, E. Burovski, P. Peterson, W. Weckesser, J. Bright, S.J. van der Walt, M. Brett, J. Wilson, K.J. Millman, N. Mayorov, A.R.J. Nelson, E. Jones, R. Kern, E. Larson, C.J. Carey, İ. Polat, Y. Feng, E.W. Moore, J. VanderPlas, D. Laxalde, J. Perktold, R. Cimrman, I. Henriksen, E.A. Quintero, C.R. Harris, A.M. Archibald, A.H. Ribeiro, F. Pedregosa, P. van Mulbregt, SciPy 1.0: fundamental algorithms for scientific computing in Python, Nat. Methods 17 (2020) 261–272. https://doi.org/10.1038/s41592-019-0686-2.
[69] Z. Pang, L. Xu, C. Viau, Y. Lu, R. Salavati, N. Basu, J. Xia, MetaboAnalystR 4.0: a unified LC-MS workflow for global metabolomics, Nat. Commun. 15 (2024) 3675. https://doi.org/10.1038/s41467-024-48009-6.

[70] J. Huerta-Cepas, F. Serra, P. Bork, ETE 3: Reconstruction, Analysis, and Visualization of Phylogenomic Data, Mol. Biol. Evol. 33 (2016) 1635–1638. https://doi.org/10.1093/molbev/msw046.
[71] C. Stringer, T. Wang, M. Michaelos, M. Pachitariu, Cellpose: a generalist algorithm for cellular segmentation, Nat. Methods 18 (2021) 100–106. https://doi.org/10.1038/s41592-020-01018-x.
[72] S. Chintala, W. Li, M.L. Lamoreux, S. Ito, K. Wakamatsu, E.V. Sviderskaya, D.C. Bennett, Y.-M. Park, W.A. Gahl, M. Huizing, R.A. Spritz, S. Ben, E.K. Novak, J. Tan, R.T. Swank, Slc7a11 gene controls production of pheomelanin pigment and proliferation of cultured cells, Proc. Natl. Acad. Sci. U. S. A. 102 (2005) 10964–10969. https://doi.org/10.1073/pnas.0502856102.
[73] R.T. Swank, M. Reddington, E.K. Novak, Inherited prolonged bleeding time and platelet storage pool deficiency in the subtle gray (sut) mouse, Lab. Anim. Sci. 46 (1996) 56–60.
[74] P.H.G.M. Willems, R. Rossignol, C.E.J. Dieteren, M.P. Murphy, W.J.H. Koopman, Redox Homeostasis and Mitochondrial Dynamics, Cell Metab. 22 (2015) 207–218. https://doi.org/10.1016/j.cmet.2015.06.006.
[75] S.A. Mookerjee, A.A. Gerencser, D.G. Nicholls, M.D. Brand, Quantifying intracellular rates of glycolytic and oxidative ATP production and consumption using extracellular flux measurements, J. Biol. Chem. 292 (2017) 7189–7207. https://doi.org/10.1074/jbc.M116.774471.
[76] O. Thaher, C. Wolf, P.N. Dey, A. Pouya, V. Wüllner, S. Tenzer, A. Methner, The thiol switch C684 in Mitofusin-2 mediates redox-induced alterations of mitochondrial shape and respiration, Neurochem. Int. 117 (2018) 167–173. https://doi.org/10.1016/j.neuint.2017.05.009.
[77] S. Mattie, J. Riemer, J.G. Wideman, H.M. McBride, A new mitofusin topology places the redox-regulated C terminus in the mitochondrial intermembrane space, J. Cell Biol. 217 (2018) 507–515. https://doi.org/10.1083/jcb.201611194.
[78] J.M. Buescher, M.R. Antoniewicz, L.G. Boros, S.C. Burgess, H. Brunengraber, C.B. Clish, R.J. DeBerardinis, O. Feron, C. Frezza, B. Ghesquiere, E. Gottlieb, K. Hiller, R.G. Jones, J.J. Kamphorst, R.G. Kibbey, A.C. Kimmelman, J.W. Locasale, S.Y. Lunt, O.D. Maddocks, C. Malloy, C.M. Metallo, E.J. Meuillet, J. Munger, K. Nöh, J.D. Rabinowitz, M. Ralser, U. Sauer, G. Stephanopoulos, J. St-Pierre, D.A. Tennant, C. Wittmann, M.G. Vander Heiden, A. Vazquez, K. Vousden, J.D. Young, N. Zamboni, S.-M. Fendt, A roadmap for interpreting 13C metabolite labeling patterns from cells, Curr. Opin. Biotechnol. 34 (2015) 189–201. https://doi.org/10.1016/j.copbio.2015.02.003.
[79] P. Pachnis, Z. Wu, B. Faubert, A. Tasdogan, W. Gu, S. Shelton, A. Solmonson, A.D. Rao, A.K. Kaushik, T.J. Rogers, J.M. Ubellacker, C.A. LaVigne, C. Yang, B. Ko, V. Ramesh, J. Sudderth, L.G. Zacharias, M.S. Martin-Sandoval, D. Do, T.P. Mathews, Z. Zhao, P. Mishra, S.J. Morrison, R.J. DeBerardinis, In vivo isotope tracing reveals a requirement for the electron transport chain in glucose and glutamine metabolism by tumors, Sci. Adv. 8 (2022) eabn9550. https://doi.org/10.1126/sciadv.abn9550.
[80] A.C. Newman, O.D.K. Maddocks, One-carbon metabolism in cancer, Br. J. Cancer 116 (2017) 1499–1504. https://doi.org/10.1038/bjc.2017.118.
[81] B.J. Gheller, J.E. Blum, E.W. Lim, M.K. Handzlik, E.H. Hannah Fong, A.C. Ko, S. Khanna, M.E. Gheller, E.L. Bender, M.S. Alexander, P.J. Stover, M.S. Field, B.D. Cosgrove, C.M. Metallo, A.E. Thalacker-Mercer, Extracellular serine and glycine are

required for mouse and human skeletal muscle stem and progenitor cell function, Mol. Metab. 43 (2021) 101106. https://doi.org/10.1016/j.molmet.2020.101106.
[82] J. Zhu, M. Berisa, S. Schwörer, W. Qin, J.R. Cross, C.B. Thompson, Transsulfuration Activity Can Support Cell Growth upon Extracellular Cysteine Limitation, Cell Metab. 30 (2019) 865-876.e5. https://doi.org/10.1016/j.cmet.2019.09.009.
[83] R. Zhang, B. Chen, L. Lin, H. Zhang, T. Luan, 13C isotope-based metabolic flux analysis revealing cellular landscape of glucose metabolism in human liver cells exposed to perfluorooctanoic acid, Sci. Total Environ. 770 (2021) 145329. https://doi.org/10.1016/j.scitotenv.2021.145329.
[84] E.A. Veal, A.M. Day, B.A. Morgan, Hydrogen Peroxide Sensing and Signaling, Mol. Cell 26 (2007) 1–14. https://doi.org/10.1016/j.molcel.2007.03.016.
[85] M.P. Murphy, How mitochondria produce reactive oxygen species, Biochem. J. 417 (2008) 1–13. https://doi.org/10.1042/BJ20081386.
[86] G.L. Semenza, HIF-1 mediates metabolic responses to intratumoral hypoxia and oncogenic mutations, J. Clin. Invest. 123 (2013) 3664–3671. https://doi.org/10.1172/JCI67230.
[87] A. Nagao, M. Kobayashi, S. Koyasu, C.C.T. Chow, H. Harada, HIF-1-Dependent Reprogramming of Glucose Metabolic Pathway of Cancer Cells and Its Therapeutic Significance, Int. J. Mol. Sci. 20 (2019) 238. https://doi.org/10.3390/ijms20020238.
[88] S. Movafagh, S. Crook, K. Vo, Regulation of Hypoxia-Inducible Factor-1a by Reactive Oxygen Species : New Developments in an Old Debate, J. Cell. Biochem. 116 (2015) 696–703. https://doi.org/10.1002/jcb.25074.
[89] O. Warburg, The Metabolism of Carcinoma Cells, J. Cancer Res. 9 (1925) 148–163. https://doi.org/10.1158/jcr.1925.148.
[90] H. Chen, A. Chomyn, D.C. Chan, Disruption of Fusion Results in Mitochondrial Heterogeneity and Dysfunction *, J. Biol. Chem. 280 (2005) 26185–26192. https://doi.org/10.1074/jbc.M503062200.
[91] A. Olichon, L. Baricault, N. Gas, E. Guillou, A. Valette, P. Belenguer, G. Lenaers, Loss of OPA1 Perturbates the Mitochondrial Inner Membrane Structure and Integrity, Leading to Cytochrome c Release and Apoptosis *, J. Biol. Chem. 278 (2003) 7743–7746. https://doi.org/10.1074/jbc.C200677200.
[92] S. Züchner, I.V. Mersiyanova, M. Muglia, N. Bissar-Tadmouri, J. Rochelle, E.L. Dadali, M. Zappia, E. Nelis, A. Patitucci, J. Senderek, Y. Parman, O. Evgrafov, P.D. Jonghe, Y. Takahashi, S. Tsuji, M.A. Pericak-Vance, A. Quattrone, E. Battologlu, A.V. Polyakov, V. Timmerman, J.M. Schröder, J.M. Vance, Mutations in the mitochondrial GTPase mitofusin 2 cause Charcot-Marie-Tooth neuropathy type 2A, Nat. Genet. 36 (2004) 449–451. https://doi.org/10.1038/ng1341.
[93] H. Chen, M. Vermulst, Y.E. Wang, A. Chomyn, T.A. Prolla, J.M. McCaffery, D.C. Chan, Mitochondrial Fusion Is Required for mtDNA Stability in Skeletal Muscle and Tolerance of mtDNA Mutations, Cell 141 (2010) 280–289. https://doi.org/10.1016/j.cell.2010.02.026.
[94] M. Frank, S. Duvezin-Caubet, S. Koob, A. Occhipinti, R. Jagasia, A. Petcherski, M.O. Ruonala, M. Priault, B. Salin, A.S. Reichert, Mitophagy is triggered by mild oxidative stress in a mitochondrial fission dependent manner, Biochim. Biophys. Acta BBA - Mol. Cell Res. 1823 (2012) 2297–2310. https://doi.org/10.1016/j.bbamcr.2012.08.007.

[95] W.J.H. Koopman, S. Verkaart, H.J. Visch, S. van Emst-de Vries, L.G.J. Nijtmans, J.A.M. Smeitink, P.H.G.M. Willems, Human NADH:ubiquinone oxidoreductase deficiency: radical changes in mitochondrial morphology?, Am. J. Physiol.-Cell Physiol. 293 (2007) C22–C29. https://doi.org/10.1152/ajpcell.00194.2006.
[96] T. Yu, J.L. Robotham, Y. Yoon, Increased production of reactive oxygen species in hyperglycemic conditions requires dynamic change of mitochondrial morphology, Proc. Natl. Acad. Sci. 103 (2006) 2653–2658. https://doi.org/10.1073/pnas.0511154103.
[97] J.P. Muñoz, S. Ivanova, J. Sánchez-Wandelmer, P. Martínez-Cristóbal, E. Noguera, A. Sancho, A. Díaz-Ramos, M.I. Hernández-Alvarez, D. Sebastián, C. Mauvezin, M. Palacín, A. Zorzano, Mfn2 modulates the UPR and mitochondrial function via repression of PERK, EMBO J. 32 (2013) 2348–2361. https://doi.org/10.1038/emboj.2013.168.
[98] S. Muliyil, M. Narasimha, Mitochondrial ROS Regulates Cytoskeletal and Mitochondrial Remodeling to Tune Cell and Tissue Dynamics in a Model for Wound Healing, Dev. Cell 28 (2014) 239–252. https://doi.org/10.1016/j.devcel.2013.12.019.
[99] A. Rakovic, A. Grünewald, J. Kottwitz, N. Brüggemann, P.P. Pramstaller, K. Lohmann, C. Klein, Mutations in PINK1 and Parkin Impair Ubiquitination of Mitofusins in Human Fibroblasts, PLOS ONE 6 (2011) e16746. https://doi.org/10.1371/journal.pone.0016746.
[100] X. Qi, M.-H. Disatnik, N. Shen, R.A. Sobel, D. Mochly-Rosen, Aberrant mitochondrial fission in neurons induced by protein kinase Cδ under oxidative stress conditions in vivo, Mol. Biol. Cell 22 (2011) 256–265. https://doi.org/10.1091/mbc.e10-06-0551.
[101] S. Verkaart, W.J.H. Koopman, J. Cheek, S.E. van Emst-de Vries, L.W.P.J. van den Heuvel, J.A.M. Smeitink, P.H.G.M. Willems, Mitochondrial and cytosolic thiol redox state are not detectably altered in isolated human NADH:ubiquinone oxidoreductase deficiency, Biochim. Biophys. Acta BBA - Mol. Basis Dis. 1772 (2007) 1041–1051. https://doi.org/10.1016/j.bbadis.2007.05.004.
[102] T. Shutt, M. Geoffrion, R. Milne, H.M. McBride, The intracellular redox state is a core determinant of mitochondrial fusion, EMBO Rep. 13 (2012) 909–915. https://doi.org/10.1038/embor.2012.128.
[103] Y.-M. Kim, S.-W. Youn, V. Sudhahar, A. Das, R. Chandhri, H.C. Grajal, J. Kweon, S. Leanhart, L. He, P.T. Toth, J. Kitajewski, J. Rehman, Y. Yoon, J. Cho, T. Fukai, M. Ushio-Fukai, Redox Regulation of Mitochondrial Fission Protein Drp1 by Protein Disulfide Isomerase Limits Endothelial Senescence, Cell Rep. 23 (2018) 3565–3578. https://doi.org/10.1016/j.celrep.2018.05.054.
[104] K.K. Griendling, D. Sorescu, M. Ushio-Fukai, NAD(P)H Oxidase, Circ. Res. 86 (2000) 494–501. https://doi.org/10.1161/01.RES.86.5.494.
[105] L.F. Ferreira, O. Laitano, Regulation of NADPH oxidases in skeletal muscle, Free Radic. Biol. Med. 98 (2016) 18–28. https://doi.org/10.1016/j.freeradbiomed.2016.05.011.
[106] K.K. Griendling, D. Sorescu, M. Ushio-Fukai, NAD(P)H Oxidase, Circ. Res. 86 (2000) 494–501. https://doi.org/10.1161/01.RES.86.5.494.
[107] S. Dikalov, Crosstalk between mitochondria and NADPH oxidases, Free Radic. Biol. Med. 51 (2011) 1289–1301. https://doi.org/10.1016/j.freeradbiomed.2011.06.033.
[108] A.E. Dikalova, A.T. Bikineyeva, K. Budzyn, R.R. Nazarewicz, L. McCann, W. Lewis, D.G. Harrison, S.I. Dikalov, Therapeutic Targeting of Mitochondrial Superoxide in Hypertension, Circ. Res. 107 (2010) 106–116. https://doi.org/10.1161/CIRCRESAHA.109.214601.

[109] A. Andrukhiv, A.D. Costa, I.C. West, K.D. Garlid, Opening mitoKATP increases superoxide generation from complex I of the electron transport chain, Am. J. Physiol.-Heart Circ. Physiol. 291 (2006) H2067–H2074. https://doi.org/10.1152/ajpheart.00272.2006.

[110] S. Kimura, G.-X. Zhang, A. Nishiyama, T. Shokoji, L. Yao, Y.-Y. Fan, M. Rahman, Y. Abe, Mitochondria-Derived Reactive Oxygen Species and Vascular MAP Kinases, Hypertension 45 (2005) 438–444. https://doi.org/10.1161/01.HYP.0000157169.27818.ae.

[111]A.S. Rambold, B. Kostelecky, N. Elia, J. Lippincott-Schwartz, Tubular network formation protects mitochondria from autophagosomal degradation during nutrient starvation, Proc. Natl. Acad. Sci. 108 (2011) 10190–10195. https://doi.org/10.1073/pnas.1107402108.

[112] L.C. Gomes, G.D. Benedetto, L. Scorrano, During autophagy mitochondria elongate, are spared from degradation and sustain cell viability, Nat. Cell Biol. 13 (2011) 589–598. https://doi.org/10.1038/ncb2220.

[113] C. Henríquez-Olguin, J.R. Knudsen, S.H. Raun, Z. Li, E. Dalbram, J.T. Treebak, L. Sylow, R. Holmdahl, E.A. Richter, E. Jaimovich, T.E. Jensen, Cytosolic ROS production by NADPH oxidase 2 regulates muscle glucose uptake during exercise, Nat. Commun. 10 (2019) 4623. https://doi.org/10.1038/s41467-019-12523-9.

[114] M.E. Sandström, S.-J. Zhang, J. Bruton, J.P. Silva, M.B. Reid, H. Westerblad, A. Katz, Role of reactive oxygen species in contraction-mediated glucose transport in mouse skeletal muscle, J. Physiol. 575 (2006) 251–262. https://doi.org/10.1113/jphysiol.2006.110601.

[115] S. Veeranki, S.C. Tyagi, Role of hydrogen sulfide in skeletal muscle biology and metabolism, Nitric Oxide 46 (2015) 66–71. https://doi.org/10.1016/j.niox.2014.11.012.

[116] M. Myszka, O. Mucha, P. Podkalicka, U. Waśniowska, J. Dulak, A. Łoboda, Sodium hydrosulfide moderately alleviates the hallmark symptoms of Duchenne muscular dystrophy in *mdx* mice, Eur. J. Pharmacol. 955 (2023) 175928. https://doi.org/10.1016/j.ejphar.2023.175928.

[117] C. Szabó, Hydrogen sulphide and its therapeutic potential, Nat. Rev. Drug Discov. 6 (2007) 917–935. https://doi.org/10.1038/nrd2425.

[118] F. Lu, S. Zhang, S. Dong, M. Wang, K. Pang, Y. Zhao, J. Huang, J. Kang, N. Liu, X. Zhang, D. Zhao, F. Lu, W. Zhang, Exogenous hydrogen sulfide enhances myogenic differentiation of C2C12 myoblasts under high palmitate stress, Heliyon 10 (2024) e38661. https://doi.org/10.1016/j.heliyon.2024.e38661.

[119] N.C. Chen, F. Yang, L.M. Capecci, Z. Gu, A.I. Schafer, W. Durante, X.-F. Yang, H. Wang, Regulation of homocysteine metabolism and methylation in human and mouse tissues, FASEB J. 24 (2010) 2804–2817. https://doi.org/10.1096/fj.09-143651.

[120] J. Lu, Z. Tang, M. Xu, J. Lu, F. Wang, X. Ni, C. Wang, B. Yu, Skeletal muscle cystathionine γ-lyase deficiency promotes obesity and insulin resistance and results in hyperglycemia and skeletal muscle injury upon HFD in mice, Redox Rep. Commun. Free Radic. Res. 29 (n.d.) 2347139. https://doi.org/10.1080/13510002.2024.2347139.

[121] Y. Zhang, L. Masters, Y. Wang, L. Wu, Y. Pei, B. Guo, A. Parissenti, S.J. Lees, R. Wang, G. Yang, Cystathionine gamma-lyase/H2S signaling facilitates myogenesis under aging and injury condition, FASEB J. 35 (2021) e21511. https://doi.org/10.1096/fj.202002675R.

[122] N.S. Misquitta, A. Ravel-Chapuis, B.J. Jasmin, Combinatorial treatment with exercise and AICAR potentiates the rescue of myotonic dystrophy type 1 mouse muscles in a sex-specific manner, Hum. Mol. Genet. 32 (2023) 551–566. https://doi.org/10.1093/hmg/ddac222.